Light Emitting Silicon Nanowires Obtained by Metal-Assisted Chemical Etching

Light Emitting Silicon Nanowires Obtained by Metal-Assisted Chemical Etching

Alessia Irrera[1*], Maria Josè Lo Faro[1,2,3], Cristiano D'Andrea[2], Antonio Alessio Leonardi[3], Pietro Artoni[3], Barbara Fazio[1], Rosaria Anna Picca[4], Nicola Cioffi[4], Sebastiano Trusso[1], Giorgia Franzò[2], Paolo Musumeci[3], Francesco Priolo[2,3,5] and Fabio Iacona[2*]

[1]IPCF-CNR, viale F. Stagno d'Alcontres 37, 98158 Messina, Italy

[2]MATIS IMM-CNR, via S. Sofia 64, 95123 Catania, Italy

[3]Dipartimento di Fisica e Astronomia, Università di Catania, via S. Sofia 64, 95123 Catania, Italy

[4]Dipartimento di Chimica, Università degli Studi di Bari "Aldo Moro", via Orabona 4, 70126 Bari, Italy

[5]Scuola Superiore di Catania, Università di Catania, via Valdisavoia 9, 95123 Catania, Italy

*E-mail: irrera@me.cnr.it, fabio.iacona@ct.infn.it

Abstract

This review reports a new process for the synthesis of Si nanowires (NWs), based on the wet etching of Si substrates assisted by a thin metal film. The approach exploits the thickness-dependent morphology of the metal layers to define uncovered nanometric Si regions which behave as precursor sites for the formation of very dense (up to 1×10^{12} NW cm^{-2}) arrays of long (up to several μm) and ultrathin (diameter of 5−9 nm) NWs. Very intense photoluminescence (PL) peaks, characterized by maxima in the 640−750 nm range and by an external quantum efficiency of 0.5%, are observed when Si NWs are excited at room temperature; spectra show a blueshift if NW size is decreased, in agreement with the occurrence of quantum confinement effects. The same etching

process can be used to obtain from a Si/Ge multi-quantum well ultrathin Si/Ge NWs which exhibit, in addition to the Si-related PL peak, a signal at about 1240 nm due to Ge nanostructures. The huge surface area of the Si NW arrays can be exploited for sensing and analytical applications. The dependence of the PL intensity on the surface chemical composition suggests indeed interesting perspectives for the detection of gaseous molecules. Moreover, Si NWs decorated with Ag nanoparticles can be effectively employed in the interference-free laser desorption-ionization mass spectrometry of low-molecular-weight analytes. A device based on conductive Si NWs, showing an intense and stable electroluminescence at an excitation voltage as low as 2 V, is also presented. The unique features of the proposed synthesis (the process is cheap, fast, maskless and compatible with Si technology) and the unusual optical properties of the material open the route towards new and unexpected perspectives of semiconductor NWs in photonics.

Keywords: silicon, nanowires, silicon photonics, photoluminescence, metal-assisted chemical etching, Raman spectroscopy, electroluminescence, pulsed laser deposition

1. Introduction

The great efforts done by a wide and extremely active scientific community to optimize the synthesis and understand the unconventional electrical and optical properties of Si nanowires (NWs) are making a concrete possibility their application in electronic devices [1], photovoltaic cells [2], and sensors [3]. Among the many peculiar properties which differentiate Si NWs from bulk Si, light emission plays a leading role, since the search for innovative Si-based materials which are light emitters at room temperature is currently considered a priority topic by both academic and industrial researchers working in the field of nanotechnology [4].

Photoluminescence (PL) from Si NWs has been reported by several papers [5-9], but its origin is controversial and reasonably due to different phenomena, ranging from the presence of N-containing complexes [5] to the phonon-assisted low temperature recombination of photogenerated carriers [6]. Very interestingly, also the radiative recombination of quantum confined excitons has been proposed to explain photon emission from this material; however, this only happens if the diameter of NWs obtained by plasma etching of a Si substrate [7, 8] or by a vapour-liquid-solid (VLS) process using a $TiSi_2$ catalyst [9] is reduced through thermal oxidation. Indeed, the main techniques currently used for Si NW synthesis cannot allow the direct formation of nanostructures having a size compatible with the occurrence of quantum confinement [10-12]. In particular, the smallest radius obtainable in NWs grown by using techniques which exploit the VLS mechanism is limited by the Gibbs-Thomson effect [13]. The effectiveness of VLS-based processes is also affected by the incorporation of the metal catalyst in the growing NWs. On the other hand, top-down approaches are widely used for NW production, but the obtaining of sizes close to those required for an efficient carrier confinement requires expensive and time-consuming (and therefore hardly compatible with industrial requirements) electron-beam lithography processes. Within this context, the metal-assisted wet etching of Si wafers, which is a two-step process usually employing an $AgNO_3$ + HF solution for the generation of Ag nanoparticles and then a HF + H_2O_2 solution for Si etching [14-17], constitutes a promising and widespread alternative, since it is a direct etching

process which does not imply the use of lithography. The approach also allows to avoid metal inclusion in the NWs, although it leads to the formation of dendrites, whose removal requires an additional etching step which could damage the nanostructures [14, 18]. However, also in this case the control of the NW size in the few-nm range represents a serious obstacle. As above discussed, the coupling of these approaches with a thermal oxidation process allows the effective production of ultrathin NWs, but the presence of an insulating SiO_2 shell may complicate the fabrication of light emitting devices in which NWs constitute the active layer, since a good electrical conduction is required for such an application.

Having as the main goal the realization of NWs with an extremely small diameter, compatible with the observation of quantum confinement effects, it is therefore clear that the most used techniques seem inadequate. In this review, we will report on the results obtained by using a modified metal-assisted wet etching process for the direct synthesis of ultrathin Si NWs [19-23]; the process is still based on the widely-employed $HF + H_2O_2$ etching solution, but it is characterized by the replacement of the $AgNO_3$ catalyst with an ultrathin metal film having a peculiar mesh-like morphology. This approach allows an outstanding control over the Si NWs structural properties; it is indeed possible to obtain NWs having diameters smaller than 10 nm. In such wires an efficient carrier confinement occurs and, as a consequence, a strong room temperature luminescence is observed under both optical and electrical excitation; an external quantum efficiency of 0.5% has been measured under optical pumping. The process is maskless, cheap and fast, and it is also compatible with Si technology, therefore suggesting new and fascinating perspectives in photonics for Si nanostructures.

We will also show that the same metal-assisted etching process can be effectively used also to etch a Si/Ge multi-quantum well (MQW) in order to produce ultrathin Si/Ge NWs [24]. In addition to the room temperature PL in the visible range, Si/Ge NWs also exhibit a PL signal in the infrared (IR) range, due to the presence of Ge nanostructures. Although the Ge-related emission is observed only at low temperature, the availability of wires in which two semiconductors,

characterized by different absorption and emission spectra, are put together may further expand the range of photonic applications of Si-based NWs.

Finally, we will describe a few possible analytical and sensing applications of Si NWs, exploiting the peculiar properties of the huge surface area of this material. The evidence that the PL signal of Si NWs exhibits a marked dependence on the surface chemical composition suggests indeed interesting applications in sensing devices [20]. Moreover, we demonstrate that Si NWs decorated with Ag nanoparticles (NPs) can be effectively employed in the interference-free laser desorption-ionization mass spectrometry (LDI-MS) of low-molecular-weight analytes [25].

2. Si NWs synthesis

Figure 1 shows a typical scanning electron microscopy (SEM) image in cross-section, obtained by using a field emission Zeiss Supra 25 microscope, of a dense array of ultrathin Si NWs, having a length of about 2.5 μm, synthetized by metal-assisted wet etching of Si wafers. The process, schematically illustrated in figure 2, employs a HF + H_2O_2 aqueous solution and it is characterized by the replacement of the salt ($AgNO_3$) typically used for the generation of the metal catalytic nanoparticles with an evaporated thin metal (Au or Ag) film, having a thickness of 10 nm or lower, characterized by a peculiar mesh-like morphology which leaves a relevant fraction of exposed Si surface [19-21]. The role of the metallic mesh consists in injecting holes into the underlying Si, so catalysing, in regions where metal and Si are in contact, Si oxidation induced by the presence of H_2O_2; the formed SiO_2 is then removed by HF, producing the sinking of the metal into Si, and hence NW formation. At the end of the process metal particles remain trapped at the bottom of the etched regions, and they can be effectively removed by a selective etching process, so that no NW contamination occurs. With respect to the use of salts, this new strategy does not imply dendrite formation and, above all, a higher control over the NW structural properties is possible. It was indeed identified the thickness range for which the morphology of the metal film can be exploited to

form Si NWs having an ultrathin diameter, compatible with the observation of quantum confinement phenomena.

Metal-assisted chemical etching was investigated in some detail by Li and Bohn, who found that a thin layer of noble metal (e.g., Au, Pt, or Au/Pd) sputtered on the surface of a Si substrate catalyzes Si etching by a solution containing HF, H_2O_2, and ethanol [26]. The chemical or electrochemical reactions occur preferentially near the noble metal [27]. Depending on the nature of the catalyst and of the substrate, it is possible to obtain NWs with different structural properties. In fact, the etching rate depends on the orientation and the doping of the substrate, and on the characteristics of the metallic mesh. It has been observed that the Si etch rate in the presence of Au is two times faster than in the presence of Ag. This difference can be attributed to the different electronegativity [26] and oxidation number of Au and Ag.

Moreover, Au always etches normal to the substrate surface, since it has a higher etching rate than Ag. Indeed, Ag can etch according to the crystallographic orientation, due to its slower etch rate. Metal-assisted chemical etching is generally isotropic and the etching occurs perpendicularly to the Si surface. However, anisotropic etching occurring along specific Si crystalline directions can be obtained by varying the relative concentration of etching and oxidizing species for Si substrates having different orientations. According to the back-bond breaking theory, it is necessary to break the back-bonds of the Si surface atoms in order to fabricate non-vertical Si nanostructures by electroless etching. The surface density of back-bonds for Si atoms is defined by the crystalline orientation and it has a minimum of two bonds for Si-(100) direction, while (110) and (111) surfaces offer three back-bonds to break. Therefore, Si etching along the (100) orientation is favored because of the lower back-bond density whatever the substrate [15]. Since the preferred etching direction is the (100), and since Si NWs synthesized by this technique are very thin, with a very high aspect ratio, in (111) substrates the formation of NW bundles can occur. This phenomenon can be attributed to surface tension forces exerted on the NWs during the drying of the sample, and it can be avoided by using super-critical CO_2 drying [28, 29].

To synthesize Si NW, p-type (B concentration of 10^{16} cm^{-3}), single crystal, (100)-oriented Si wafers were cut into fragments having an area of about 1 cm^2 and then UV oxidized and dipped in diluted HF to obtain clean and oxide-free Si surfaces. Afterwards, the Si samples were covered by a thin Au (thickness of 2 or 3 nm) or Ag (thickness of 10 nm) layer, deposited at room temperature by electron-beam evaporation (EBE) of high purity (99.99%) metal pellets. Film thickness was determined by Rutherford backscattering spectrometry measurements. The metal-covered Si samples were etched at room temperature in an aqueous solution of HF (5 M) and H_2O_2 (0.44 M) to form Si NWs. NW length was varied in the 1-7 μm range; depending on the doping level of the substrate, etch rate values range from 250 to 500 nm min^{-1}. Finally, the removal of the Au or Ag particles was carried out by dipping the sample in a KI + I_2 aqueous solution. The whole process works at room temperature.

The key point of the process which allows to obtain ultrathin NWs is the correlation between the thickness of the metal films and the size of the Si regions which remain uncovered due to the nanoscale-morphology of the films. Figure 3(a) shows a SEM image of a Si surface after the deposition of 3 nm of Au. Dark regions are uncovered Si, while Au is present in the yellowish regions. Several nanometric uncovered Si areas, almost circular and totally embedded within Au regions, are present, and they are indeed the precursor sites where NWs will form upon etching. Ag films qualitatively behave in the same way, but they exhibit a greater tendency to balling up than Au, and therefore thicker layers are needed to obtain a morphology similar to that shown in figure 3(a). Figure 3(b) presents a statistical analysis of the size of the uncovered Si sites detected in SEM images recorded after the deposition of 10 nm of Ag or 2 or 3 nm of Au. All size distributions are Gaussian-shaped and have mean diameters ranging from 6 to 12 nm, with smaller sites achieved for Au with respect to Ag and by increasing the amount of deposited Au.

The process is maskless, cheap, fast (the array of NWs having a length of about 2.5 μm shown in figure 1 is prepared in less than 10 minutes) and compatible with Si technology, so that it could be employed also for applications of Si nanostructures in an industrial environment.

3. Structural characterization of Si NWs

Figure 4 reports a cross section SEM image of a uniform array of Si NWs, having a length of about 3 μm and very small diameters, synthesized by the metal-assisted wet etching technique above described. With respect to the image shown in figure 1, here the sample has been slightly tilted with respect to the electron beam, and this expedient allows to highlight the extremely high NW areal density. The density of the NW array can be appreciated even better in the plan view SEM image shown in figure 5. The quantitative analysis of several plan view SEM images gives density values higher then 1×10^{12} NW cm^{-2}, corresponding to a coverage of about 60%. This density is significantly higher than the typical values found for Si NWs grown by techniques based on the VLS mechanism; furthermore, in agreement with the etching mechanism described in the previous section, the value mirrors the density of the precursor sites defined by the Au mesh shown in the SEM image in figure 3(a). No metallic residues are detected in both cross section and plan view SEM images.

By analysing the SEM plan view image shown in figure 5 the surface coverage is estimated to be approximately 60%; remarkably, the same surface coverage is found by analysing SEM images taken at different magnifications, indicating scale invariance in the high-density 2D arrangement of the Si NW array. This particular texture is obtained owing to the peculiar structure of the thin Au layer, which is close to the 2D percolation threshold (filling fraction 54%) on a Si surface. It is well known that an infinite cluster is a fractal object in the vicinity of the percolation threshold. The Au morphology is imposed on the Si substrate as a negative mask during the wet etching procedure; as a consequence, the Si NW distribution is organized with a fractal structure. A fractal dimension D of 1.87 was calculated, corroborating the claim of a dense planar arrangement of the Si NW array, which is exactly what it is expected starting from a percolation Au film [30]. A strong correlation between the optical properties and the fractal characteristics of Si NWs has been very recently demonstrated. In fact, the fractal array promotes a high light-trapping efficiency with

total reflectance values down to 0.1% when the incident wavelength matches the maximum heterogeneity size exhibited by the fractal arrangement of Si NWs. Furthermore, a strongly enhanced Raman emission, due to multiple scattering processes, is shown to depend on the effective wavelength resonantly matching the heterogeneity sizes of the Si NW 2D fractal arrangement [30].

NW diameter is too small to be measured by SEM, so that this information has been obtained by Raman measurements. Micro-Raman spectra have been collected by exciting with the 364 nm line of an Ar^+ laser; this wavelength has been selected due to its low depth penetration in Si (about 12 nm), which allows to eliminate the spectral contribution of the Si substrate. Heat-induced artefacts have been prevented by using a low power (4 μW) for measurements. Figure 6 reports the Raman spectra of Si NWs synthesized by exploiting the catalytic activity of thin Ag (10 nm thick) or Au (2 and 3 nm thick) layers; in agreement with literature data dealing with quantum confined crystalline Si nanostructures [31] peaks are asymmetrically broadened and redshifted with respect to the symmetric and sharper peak of bulk crystalline Si, shown at 520 cm^{-1} in the same figure. The peaks have been fitted by using a phenomenological model which has been initially used to deduce the size of Si nanocrystals (ncs) from their Raman spectrum [32, 33] and recently extended also to Si NWs [34]. The results of the fit procedure give diameters of 9 ± 2 nm for NWs synthetized by using 10 nm of Ag, 7 ± 2 nm for the 2 nm thick Au film and 5 ± 1 nm for the 3 nm thick Au film. It is remarkable that the diameters provided by the analysis of the Raman spectra coincide with the size of the Si precursor sites defined by the metallic films employed as catalysts (see the SEM image reported in figure 3(a) for an example), confirming that the proposed synthesis operates by directly reproducing, without using any lithographic process, the thickness-dependent nanoscale morphology of thin metal films on the etched Si wafers.

Transmission electron microscopy (TEM) measurements performed on single NWs scratched from the substrate and collected on a Cu grid demonstrated that metal-assisted wet etching leads to the formation of monocrystalline and defect-free NWs. Although this characteristic may appear an almost obvious consequence of the nature of the synthesis process, it represents a

relevant advantage with respect to wires grown by exploiting the VLS mechanism or fabricated by a lithographic approach. TEM measurements also evidenced that NWs have a core-shell structure; the cores are made by crystalline Si (as demonstrated by the presence of Si lattice planes in high resolution images) and the measured diameters are in very good agreement with the size estimated by Raman measurements [19]. The shells are amorphous and quite irregular and, as demonstrated by the energy filtered TEM technique [19], they are essentially composed by SiO_2, formed due to a chemical reaction involving NW surface and the atmospheric oxygen; the typical thickness of the shell accounts for about 1-2 nm.

4. Photoluminescence properties of Si NWs

A great advantage of Si NWs is the possibility to grow them via a self-assembling method based on the VLS mechanism [10], which exploits a catalytic agent, usually metal nanoclusters. The catalyst promotes an axial growth under the metallic droplets if the substrate is maintained at a specific temperature able to form a liquid eutectic. This technique gives the possibility to control the size, length, composition and crystalline quality of the NWs thus determining their optical and electrical properties. Some groups reported Si NW growth by different physical mechanisms (oxide-assisted growth [35] or the vapor-solid-solid method [36]), but the VLS technique remains the most extensively used. Au is the most widely chosen catalyst in this approach, due to its capability to form an Au/Si eutectic at a very low temperature (363 °C). The growth of Si NWs by the VLS method exploits many different synthesis techniques to supply the Si vapor phase, including chemical vapor deposition [37-39], molecular beam epitaxy (MBE) [40, 41] and evaporation [42, 43]. The use of a metallic catalyst represents one of the main drawbacks of this approach. Indeed, the presence of traces of Au inside the NWs introduces trapping levels in the Si bandgap, acting as nonradiative recombination centres and, therefore, drastically limiting the efficiency of the light emission process. Moreover, the Gibbs-Thomson effect predicts the existence of a critical radius for the growth of wires by the VLS mechanism; indeed, for NW whose size is below this threshold the

growth is inhibited. The value of the critical radius depends on the growth conditions and typically accounts for tens of nm [44]. Consequently, it is impossible to observe quantum confinement and light emission in Si NWs grown by the VLS technique, unless subsequent thermal oxidation processes are employed to reduce their size [9]; however, a precise control of oxidation processes in NWs is still lacking, owing to both their large surface/volume ratio and to the presence of the metal contamination, acting as a catalyst for the longitudinal oxidation.

Peng et al. pioneered fabrication of Si NW templates using metal-assisted chemical etching by placing a Si substrate in a solution containing $AgNO_3$ and HF [45]. A relevant advantage of this approach is the absence of Au inclusion inside the NWs. Moreover, NW doping does not require additional process steps but it depends only on the substrate doping; indeed, starting from a properly doped wafer, it is possible to obtain NWs with a prefixed and well controlled level of doping [46, 47]. The structure of the NWs prepared by using Ag salts depends on the spacing and size of Ag clusters precipitated from the $AgNO_3$ solution and NWs with mean radius typically ranging between 30 and 200 nm can be obtained [48-50]. For this reason quantum confinement effects cannot occur. Metal-assisted chemical etching also allows the realization of ordered NW arrays by using different types of masks [51-53]. Also in this case the obtained NWs have a radius too large to exhibit quantum confinement effects, because the smaller feature realizable by lithography processes (including polystyrene nanospheres lithography, interference lithography, electron beam lithography, and silica colloids lithography) limits the NW size [51-54]. Only a few works report the use of Ag thin films as a catalyst without the use of masks [55, 56], but no PL emission is demonstrated. Moreover, in the case of non-patterned metal films the variation and control of the NW diameter has never been reported, while these results have been obtained by using masks [53]. Some attempts to obtain Si NWs by using Au films (without masks) have been performed [52, 55], but they did not succeed. The tuning of the PL emission of Si NWs fabricated by using a mask and an Ag layer as a catalyst was reported [57], but no variation of the PL spectra

as a function of the size of the pillars was obtained, since the pillar diameter largely exceeds the size needed to observe quantum confinement effects in Si.

Recently, various hybrid systems containing Si NWs and exhibiting PL emission at room temperature due to surface state or defects have been proposed [58]. Different materials including metals, semiconductors, dielectrics have been employed to realize such hybrid systems [59-65]. Si NWs decorated with Ag islands exhibit a PL emission due to the surface defects related to the sample production. The presence of the Ag islands determines an enhancement of the PL efficiency that it is possible to explain in terms of radiative energy exchange between NW and metal NPs due to enhanced exciton–plasmon radiative coupling [66]. Moreover, a hybrid system consisting of Si NWs decorated with ZnO nanoclusters, exhibiting light emission in the 400-800 nm range, was realized by CVD [65].

Finally, by excluding some reports where the observed PL emission is clearly not related with quantum confinement, since the investigated nanostructures are too large [5, 6], room temperature PL reasonably due to excitonic recombination in confined nanostructures has been claimed for NWs whose size was reduced by additional oxidation processes [7, 8]. On the other hand, metal-assisted wet etching allows the direct synthesis of Si NWs which are light emitters at room temperature, since their size is compatible with the observation of quantum confinement effects.

Figure 7(a) reports the room temperature PL spectra of Si NWs having a length of about 2.5 μm. NWs were realized by using p-type Si substrates (100) having a resistivity of 1.5 Ω cm. A thin Au layer, having a thickness of 2 or 3 nm, was deposited on the Si samples at room temperature by EBE, by using high purity (99.99%) pellets as a source. Alternatively, a 10 nm thick Ag layer was deposited with the same procedure. Finally, metal-covered Si samples were etched at room temperature in an aqueous solution of HF (5 M) and H_2O_2 (0.44 M) to form Si NWs. The etching process realized by using 2 or 3 nm of Au determines a mean NW diameter of 5 and 7 nm, respectively, while by using a film of 10 nm of Ag the mean diameter of NWs is 9 nm [19]. The PL

measurements are obtained by exciting with the 488 nm line of an Ar^+ laser at a pump power of 10 mW. The laser beam was chopped by an acousto-optic modulator at a frequency of 55 Hz. PL signals were analysed by a single-grating monochromator and detected by a H_2O-cooled photomultiplier tube. All spectra consist of a broad band having a full width at half maximum of about 150 nm; it is particularly noteworthy that the wavelength corresponding to the maximum of the PL peak depends on the NW mean size. In particular, the peak is centred at about 750 nm for NWs having a mean diameter of 9 nm, while it is blueshifted at about 690 nm for a mean diameter of 7 nm, and further shifted at 640 nm for a size of 5 nm. This dependence strongly resembles the well-known behaviour of Si ncs [4, 21, 67], suggesting that, also in this case, quantum confinement effects are responsible for the light emission; further evidences supporting this interpretation will be given in the following of this section.

Time-resolved PL measurements have been used to gain a deeper comprehension of the mechanisms ruling the light emission process in Si NWs. Measurements were performed by monitoring the decay of the room temperature PL signal after pumping to steady state and switching off the laser beam. The overall time resolution of the system is 200 ns. The decay curves of the PL signal measured at the wavelengths corresponding to the maxima of the peaks shown in figure 7(a) are reported in figure 7(b). Curves have a stretched exponential shape and lifetime (τ) values range from 17 μs at 640 nm to 38 μs at 750 nm. The observation of faster decays for shorter wavelengths resembles the behaviour previously reported for Si ncs [68, 69]; note that the measured τ values are two orders of magnitude longer than those reported for Si pillars produced by electron-beam lithography and subsequently thinned by thermal oxidation [7], demonstrating the superior structural quality of NWs synthesized by metal-assisted etching. PL emission is very bright and clearly visible to the naked eye, as demonstrated by figure 7(c) which displays a photograph of the homogeneous red emission coming from a Si NW array excited by the 364 nm line of a fully defocused Ar^+ laser.

In order to estimate the PL efficiency of Si NWs, their spatial emission profile in the far-field has to be determined. Figure 8(a) reports the integrated PL intensity as a function of the emission angle θ, as measured by optically pumping at 405 nm the Si NWs at a fixed excitation angle with respect to the sample surface. The angular dependence of the PL intensity can be very well fitted by a cosine function (red line in the figure), which demonstrates that Si NWs behave as a perfect Lambertian source. This allows us to estimate the total PL emission of the Si NWs by measuring the light emitted within a given solid angle around normal direction, and then weighting it to the total emission power of a Lambertian source. The PL power efficiency is then given by the ratio between the total PL emission power and the absorbed excitation power.

According to the emission properties of a Lambertian source, the total emission intensity I_{tot} is:

$$I_{tot} = 2I_{\max}\int_0^{\pi/2}\int_0^{2\pi}\cos(\theta)\sin(\theta)d\theta d\varphi = 4\pi I_{\max}\int_0^{\pi/2}\cos(\theta)\sin(\theta)d\theta = 2\pi I_{\max}$$

On the other hand, for the same source, the light emission intensity collected within a solid angle of angular aperture 2α around the normal direction will be:

$$I_{2\alpha} = I_{\max}\int_0^{\alpha}\int_0^{2\pi}\cos(\theta)\sin(\theta)d\theta d\varphi = 2\pi I_{\max}\int_0^{\alpha}\cos(\theta)\sin(\theta)d\theta = \pi I_{\max}[1-\cos^2(\alpha)]$$

Thus, if $P_{2\alpha}^{\exp}$ is the PL power measured within a solid angle of angular aperture 2α around the normal direction and P_{exc} is the absorbed excitation power, the PL external power efficiency will be given by:

$$\eta_P = \frac{P_{2\alpha}^{\exp}}{P_{exc}}\frac{I_{tot}}{I_{2\alpha}} = \frac{P_{2\alpha}^{\exp}}{P_{exc}}\frac{2}{[1-\cos^2(\alpha)]}$$

Figure 8(b) shows the measured power efficiency curve of Si NWs as obtained by optically exciting at 405 nm the sample and collecting the PL emission with an objective lens of numerical aperture = 0.4 = sinα. Under the conservative assumption that the 405 nm exciting laser beam is totally absorbed by the Si NWs, it is obtained from the experimental data:

The external quantum efficiency η_Q is then obtained by normalizing η_P to the photon fluxes of the excitation and emission beams:

A lower limit estimate of the external quantum efficiency is hence 0.5%. This value is comparable with the best efficiencies reported in literature for porous Si [70] and Si ncs [71].

Figure 9 displays the room temperature PL spectra, obtained by exciting the system at 364 nm, of Si NWs having the same diameter of 7 ± 2 nm but different lengths, ranging from 1.3 to 6.8 μm. The PL intensity strongly increases by increasing the NW length. Indeed, each NW allows multiple electron-hole recombinations and therefore, by increasing the length, the number of the electron-hole pairs created by the laser pump inside a single NW also increases. However, by analysing the dependence of the PL intensity on the NW length, it is evident that intensity tends to saturate by increasing the length. This phenomenon is due to the excitation conditions; in fact, in our experimental setup the laser spot illuminates a fixed volume. For smaller NWs, the illuminated volume is sufficient for the complete excitation of the sample, while by increasing the length only a fraction of the NWs is illuminated, determining the saturation of the PL signal. This experiment highlights an important advantage of NWs with respect to other Si-based luminescent nanomaterials, such as Si ncs. In fact, an increase of the electron-hole pair density in Si ncs, due to their small volume, corresponds to a higher probability to have nonradiative effects (i.e. Auger processes); on the other hand, the probability to have nearby electron-hole pairs in NWs is small and further decreases by increasing their length, and therefore nonradiative phenomena are strongly reduced.

The PL properties of the Si NW arrays have been also studied as a function of the flux of 488 nm photons. Data are reported in figure 10(a); the integrated PL intensity increases with the

photon flux throughout the explored range, although at high fluxes a marked saturation occurs. To understand the reasons leading to the saturation of the PL signal, the lifetime of the PL signal at 690 nm at different photon fluxes was measured; the decay curves shown in figure 10(b) demonstrate that no appreciable variation of the lifetime occurs, since a constant value of 20 μs is found in all cases. The analysis of the data in figure 10 indicates that nonradiative processes, such as Auger recombination, do not play a relevant role in competition with photon emission.

Important information about the optical properties of Si NWs can be obtained by measuring the risetime τ_{on} of the PL signal as a function of the pump power. The experiment was realized by monitoring the increase of the PL signal at 690 nm up to steady state after switching on the excitation laser beam, and it allows the calculation of the excitation cross section σ of the system [67]. In fact, τ_{on} is given by:

$$\frac{1}{\tau_{on}} = \sigma\phi + \frac{1}{\tau} \qquad (1)$$

where ϕ is the pumping photon flux and τ is the lifetime. By plotting the reciprocal of the τ_{on} values (which typically account for a few μs) as a function of ϕ and by a linear fit of the data, it is obtained $\sigma = 5\times10^{-17}$ cm^2 [19], a value very close to those previously reported for Si ncs [67, 72]; this evidence strongly supports the view that the PL from Si NWs is due to the radiative recombination of quantum confined excitons.

The temperature dependence of the PL signal can provide further hints about the mechanism of the photon emission process in Si NWs, as well as useful information about the potentialities of this material for practical applications, since it is well known that in Si-based materials a strong temperature quenching of the PL may occur [73]. Figure 11(a) reports the PL intensity (I_{PL}) at 690 nm as a function of the temperature; in the investigated range (11–300 K) a monotonic increase of I_{PL} with the temperature is observed up to about 270 K, where the maximum intensity is detected, while for higher temperatures a slight decrease occurs. The overall dependence of I_{PL} on

temperature is quite weak, since the intensity change on going from 11 to 270 K is smaller than a factor of 10.

Figure 11(b) reports the values of the PL lifetime obtained at different temperatures in the 11–300 K range. The figure shows that τ, measured at a wavelength of 690 nm, decreases by about one order of magnitude by increasing the temperature, from 200 μs at 11 K to 20 μs at room temperature. A similar behaviour has been previously observed in Si ncs [74, 75] and porous Si [76], so that also this experiment confirms that quantum confinement effects are operating in Si NWs.

It has been previously demonstrated [75] that, by solving the appropriate rate equation, I_{PL} is given by equation (2):

$$I_{PL} \propto \sigma\phi \frac{\tau}{\tau_{rad}} N \qquad (2)$$

where N is the total population of emitting centres and τ_{rad} the radiative lifetime; in equation (2) the luminescence decay time τ includes both radiative and nonradiative processes. In the low pump power regime, I_{PL} increases linearly with ϕ and it is proportional to the ratio τ/τ_{rad}. Since N and σ do not depend on temperature, the only temperature dependences are due to τ and τ_{rad}. If nonradiative processes occurs, τ does not coincide with τ_{rad} and I_{PL} depends on temperature. The radiative rate ($R_R = 1/\tau_{rad}$), obtained for different temperatures from the ratio between I_{PL} and τ at a fixed photon flux, is shown in figure 11(c). R_R increases by about a factor of 200 on going from 11 to 300 K, and this effect is partially counterbalanced by a more significant role of the fast nonradiative processes, as indicated by the marked lifetime shortening shown in figure 11(b) for the same temperature range.

The dependence of R_R on temperature can be explained by using a model initially developed for porous Si [76] and then applied also to Si ncs [74, 75]. According to this model, the excitonic levels are split by an energy Δ due to the electron-hole exchange interaction. The lower level corresponds to a triplet state which is threefold degenerate and has a radiative decay rate R_T, while

the upper level is a singlet state and has a radiative decay rate R_S. Once excited the excitonic population will be distributed according to thermal equilibrium law. Hence at a temperature T the radiative decay rate will be given by equation (3):

$$R_R = \frac{3R_T + R_S \exp\left(-\frac{\Delta}{kT}\right)}{3 + \exp\left(-\frac{\Delta}{kT}\right)} \qquad (3)$$

The relative population of the singlet state increases by increasing temperature and, since R_S is much higher than R_T (the transition from a triplet state is parity forbidden), also the total radiative rate will consequently increase. Equation (3) can be used to fit the data in figure 11(c); the fit is shown as a continuous line and it gives $\Delta = 26.9 \pm 4.3$ meV, a value in good agreement with those experimentally found for porous Si [76] and Si ncs [74, 75], and also with the splitting found in Si NWs by first-principles calculations [77], further supporting the view that quantum confinement effects are operating in Si NWs.

5. Synthesis and optical properties of Si/Ge NWs

Si/Ge NWs were realized by etching a Si/Ge MQW grown by MBE on a Si substrate at 450 °C, consisting of alternating Si (54 nm thick) and Ge (1 nm thick) layers deposited at a rate of 0.3 and 0.01 nm s^{-1}, respectively. The Si/Ge stack was repeated 62 times, giving a total thickness of about 3.5 μm. Sample structure is depicted in figure 12. Si/Ge NW formation was accomplished by using the same process described in section 2 for pure Si NWs. After the cleaning steps, a 2 nm thick Au layer was deposited on the MQW at room temperature by EBE of high purity (99.99%) Au pellets. Au-covered samples were then etched at room temperature at a rate of 130 nm min^{-1} in an aqueous solution of HF (5 M) and H_2O_2 (0.44 M) to form Si/Ge NWs. Au removal was carried out by a dip in an aqueous solution of KI and I_2.

Figure 13 reports cross section SEM images displaying the dense (about 10^{12} NW cm^{-2} can be counted in plan view SEM images) and uniform Si/Ge NW arrays obtained by following the

above procedure; the length ranges from 1.0 to 2.7 μm and linearly depends on the etching time. NWs still maintain the MQW structure; indeed, in the SEM images the bright regions are associated to the presence of Si, while the dark regions correspond to the Ge wells. A mean diameter of about 8 nm has been determined by Raman measurements according to the procedure described in section 3 and confirmed by TEM analysis of several NWs scratched from the substrate.

Under excitation with 488 nm photons Si/Ge NWs exhibit an intense room temperature PL signal due to quantum confined Si nanostructures, as shown in figure 14(a) for NWs with a length of 2.7 μm; the spectrum consists of a broad band centred at about 670 nm, very similar to the emission of pure Si NWs reported in figures 7(a) and 9. Analogously to the behaviour shown in figure 9 for the case of Si, a similar PL spectrum, although less intense, was observed in shorter Si/Ge NWs.

Figure 14(b) reports the PL spectra in the IR region of Si/Ge NWs, recorded at temperatures ranging from 11 K to to room temperature. The spectra show that no Ge-related PL signals are detected at room temperature, but a peak centred at about 1240 nm becomes appreciable if the temperature is lowered down to 100 K and reaches its maximum intensity at 11 K. The peak position corresponds to literature data dealing with luminescent Ge nanostructures [78-80]. Furthermore, it can be noticed that the PL emission exhibits a blueshift by decreasing temperature, in agreement with the well-known dependence of the Ge bandgap on temperature. The increase of the PL intensity at low temperature depends on a reduced efficiency of nonradiative phenomena. It is noteworthy that the emission at 11 K is about 5 times stronger than that one observed at the same temperature in the unetched MQW, indicating that a higher degree of confinement is present in the NWs, where Ge regions can be indeed assumed to be nanodots, with respect to the MQW. By also considering that NWs cover about 50% of the sample surface, the actual enhancement factor of the PL intensity for Si/Ge NWs is higher and accounts for at least an order of magnitude. Note finally that the intensity of the Si-related PL signal from Si/Ge NWs reaches a maximum at about 270 K

and then strongly decreases by decreasing the temperature, analogously to the temperature dependence shown in figure 11(a) for pure Si NWs.

Figure 15 reports the time-decay curves of the Ge-related PL signal at 1220 nm obtained at different temperatures. Decays cannot be fitted by a single exponential function and the τ values decrease from 7.0 μs at 11 K to 0.6 μs at 80 K. This behaviour clearly indicates that fast nonradiative phenomena, such as Auger processes or thermally activated quenching processes [81], influence the de-excitation of Si/Ge NWs. The efficiency of such processes increases with the temperature, producing the complete quenching of the Ge emission observed at room temperature.

Although Si/Ge NWs were previously successfully synthesized by using an Au-catalysed MBE growth [82] or a metal-assisted etching process [83], to our knowledge the above data constitute the first evidence of simultaneous light emission both in the visible and in the IR regions from such kind of NWs. Very recently the same double emission has been obtained also in a hybrid system consisting of Si NWs infiltrated with C nanotubes. This hybrid system based on Si NWs and C nanotubes, although its synthesis and its handling may appear complicated at first glance, maintains a good compatibility with Si technology and has the additional advantage to exhibit also the IR emission at room temperature [84].

6. Sensing and analytical applications of Si NWs

Previously proposed applications of Si NWs as sensors are mainly based on the variation of the electrical properties due to the exposure to reactive gases [3]. On the other hand, luminescent NW arrays fabricated by metal-assisted wet etching offer the additional possibility to exploit changes in the intensity or on the wavelength of the emitted light for the same scope. The sensing potentialities of Si NWs have been firstly evaluated by simply following the evolution of the PL signal as a function of the exposure to air, where reactive gases such as O_2 or H_2O are present. Figure 16 reports the intensity of the PL signal at 690 nm, obtained by exciting at 488 nm freshly prepared Si

NWs, as a function of the air exposure time at room temperature. PL intensity monotonically increases with the exposure time; at the end of the experiment (245 days since NW synthesis) PL intensity is stronger than the initial one by a factor of 250, while no remarkable variation of the peak position and shape occur.

Since in quantum confined Si nanostructures an efficient surface passivation is required in order to suppress the nonradiative de-excitation channels which limit the efficiency of the light emission process, the observed dependence of the PL intensity on the air exposure time can be reasonably explained by an improved NW passivation, determined by heterogeneous chemical reactions between the freshly etched Si surface and atmospheric gases such as O_2 or H_2O, leading to the formation of Si-H, Si-O or Si-OH bonds [85]. This interpretation has been confirmed by the observation that the lifetime of the PL signal increases with the air exposure time; in particular, while lifetime values lower than 10 μs characterize NWs exposed to air for a few days, a value of about 30 μs has been observed in 245-days-aged samples. The slower lifetime which characterizes the strongly luminescent NW samples obtained for long exposure times demonstrates that the interaction with air indeed produces an efficient surface passivation of the quantum confined NWs, and, in turn, a reduction of the centres for nonradiative recombination.

Note that the same gas-solid reactions which produce NW passivation could also determine the formation of new surface luminescent centres, such as siloxene and its derivates [86]. However, this hypothesis, which essentially neglects the role of quantum confinement in the luminescence from Si NWs, appears inadequate to explain the observed dependence of the PL signal on the air exposure time, since the formation of new surface emitting centres cannot imply the variation of the lifetime of the PL signal which unambiguously characterize our experiments.

It has also to be remarked that the absence of saturation of the PL intensity in the explored time range (the trend in figure 16 is roughly linear for the whole time lapse) clearly evidences the huge surface area of Si NWs, further highlighting the great potentialities of this material for the fabrication of sensors.

The effect of passivation on the PL properties of Si NWs has been also investigated by following the variation of the PL intensity at 690 nm during a prolonged exposure to 488 nm photons at a power of 10 mW. The left part of figure 17 demonstrates that a PL intensity enhancement accounting for about a factor of 1.5 is observed if the laser is left for a time lapse of 2000 s on the sample kept in air; no steady state is reached, even if the experiment is prolonged. In agreement with the picture described in the first part of this section, laser irradiation accelerates the decomposition rate of the O_2 and H_2O molecules adsorbed on the NW surface and therefore increases the rate of the reactions leading to NW passivation. Since also laser-induced desorption simultaneously occurs, the increase of the PL signal shown in figure 17 is the result of the competition between the two effects and it is therefore slower than that reported in figure 16, where no phenomena competing with passivation are active.

After the 2000 s laser exposure in air, if NW irradiation is continued in vacuum at a pressure of about 10^{-5} Torr, the PL signal at 690 nm decreases, as shown in the right part of figure 17. While laser irradiation in air increases the rate of the reactions leading to NW passivation, no formation of surface oxidized species occurs during irradiation in vacuum and therefore desorption becomes the only operating effect; in absence of an efficient surface passivation, nonradiative recombination limits the PL efficiency of the NWs. The relevance of nonradiative processes in samples irradiated in vacuum is confirmed by the shortening of the PL lifetime. It is interesting to note that at the end of the experiment the PL signal is weaker than that initially measured, demonstrating that laser irradiation in vacuum is able not only to cancel the effect of the previous irradiation in air, but also to partially remove the pre-existing NW passivation.

Another interesting approach to exploit NWs for analytical and sensing applications exploits decoration with metal (Ag, Au) NPs. An example of a Si NW array decorated with Ag NPs is shown in the cross section SEM image reported in figure 18(a). The complete, dense, and uniform decoration of Si NWs is performed by pulsed laser deposition. The process is realized in a high vacuum chamber with a residual pressure of 7×10^{-7} Torr. The laser beam from a KrF excimer laser

(25 ns pulse width, 248 nm wavelength, 10 Hz repetition rate) is focused onto the surface of a pure Ag target using a quartz lens. The laser fluence is set at 2.0 J cm^{-2}. To fully decorate the NW surface from the top to the base, a deposition cycle consisting of 60000 laser pulses was carried out. The higher resolution SEM images reported in figure 18(b)-(d) refer to the top (b), center (c) and bottom (d) regions of a decorated NW, and allow to better appreciate that NWs are very uniformly covered with NPs throughout their length; the almost spherical shape, the high density and the very small size (radii generally fall into the 5-10 nm range) of Ag NPs are also noteworthy. The uniform Ag coverage of NWs is also confirmed by the TEM image reported in figure 18(e), where metal NPs are visible as dark spots.

A very interesting application for NP-decorated NWs is the surface-enhanced Raman spectroscopy detection of very low concentrations of organic molecules. In fact, Ag NPs are able to strongly enhance the Raman signal of molecules attached on their surface through a localized plasmon resonance phenomenon [87, 88]. Another intriguing application for NP-decorated NWs is the interference-free LDI-MS of low-molecular-weight analytes. Matrix-assisted LDI is a soft ionization method widely employed in MS applications for the identification of large molecules (> 1000 Da) [89]. In this technique, organic compounds are generally used to desorb/ionize target molecules for their analysis. Unfortunately, in the mass range below 1000 Da, such matrixes produce numerous interfering ion adducts making them poorly useful for the MS characterization of small analytes (e.g. sugars, amino acids, fatty acids, drugs). As a result, nanostructured surfaces have emerged as valid alternatives in matrix-free LDI-MS applications [90]. Among different nanomaterials, Si NWs have proven particularly appealing as new analytical platforms [90, 91]. In 2005 these nanostructured surfaces have been first proposed [92] as an evolution of porous Si, already applied in LDI-MS [93]. Si NWs represent an efficient evolution of porous Si as they show similar or improved features such as optimal UV laser light absorption, antireflectivity [94, 95], high surface area and NW density [92, 94]. For example, it was observed that Si NWs require a reduced laser fluence for ion production as compared to conventional matrixes [96] giving higher

signal intensity and better signal-to-noise ratio. Several groups have developed Si-based nanostructured surfaces following different strategies including metal-assisted wet-chemical etching [94, 95, 97, 98] and VLS growth [95, 99].

Ag-decorated Si NWs display good performances for the analysis of molecules bearing unsaturated bonds exploiting the affinity of Ag towards them. In particular, such substrates are extremely efficient for the detection of squalene, oleic acid and other compounds [25, 100], even in real food samples (e.g. oils). Figure 19 provides an example of the interference-free MS spectrum of oleic acid in acetone obtained using a Si NW array decorated with Ag NPs. As shown by the isotopic pattern evidenced in the inset of the figure, oleic acid is detected as an adduct with Ag ions emitted from the NPs of the Ag/Si NW platform. Other studies are in progress on the application of Au NPs-decorated Si NW arrays for the detection of small molecules in complex matrixes, such as body fluids.

7. Electroluminescent devices based on Si NWs

The capability of Si NWs to emit photons under electrical excitation, and therefore their potentialities to constitute the active region in a Si-based light source operating at room temperature to be employed in Si nanophotonics, has been tested by fabricating simple prototype devices.

NW arrays were obtained by following the procedure described in section 2. Highly doped p-type (B concentration of 1.5×10^{20} cm^{-3}, corresponding to a resistivity of 8×10^{-4} Ω cm) single crystal, (100)-oriented Si wafers were used in the etching process in order to obtain conductive NWs. Etching times were set in order to get lengths ranging from 2 to 5 μm, the NW diameter was fixed at 7 ± 2 nm by a proper selection of the metal catalyst and the density was about 10^{12} cm^{-2}. The NW arrays were covered by a transparent conductive layer of aluminum zinc oxide (AZO), having a resistivity of 0.09 Ω cm and a thickness of 1.3 μm, deposited by RF magnetron sputtering. The device structure is depicted in figure 20(a): AZO is a n-type material which forms a p-n junction with the underlying p-type NW array. Furthermore, AZO allows current injection in the

device without absorbing the emitted photons, being characterized by a transmittance of about 85% in the spectral range 480–1300 nm. The back electrical contact of the device was realized by sputtering a 900 nm thick Au layer on the backside of the Si substrate. A detail of the device structure, showing the AZO/NWs interface, is visible in the SEM cross section reported in figure 20(b).

A preliminary characterization of the emission of these devices has been performed by using emission microscopy (EMMI) measurements. The EMMI apparatus consists of an optical microscope and a CCD camera sensitive to visible and IR radiation (from 0.3 to 1.2 μm), surrounded by a shielding box. The EMMI image obtained by biasing a device based on Si NWs is reported in figure 21 and reveals an intense and stable emission over the whole device area. In the image the intensity is reproduced in a colour scale.

Electroluminescence (EL) measurements have been performed by biasing the device with a DC regulated power supply. Light emitted from an area of 0.04 mm^2 has been collected through a 20× microscope objective, and then sent to a grating spectrometer equipped with a liquid N_2-cooled Si CCD detector. The EL spectra of a device based on Si NWs having a length of about 2.5 μm, forward biased at voltages ranging between 2 and 6 V, are shown in figure 22(a). The current which flows through the device is of the order of 1 A/cm^2 and increases with the applied voltage. EL spectra consist of a broad peak centred at about 700 nm; its position and shape resemble those of the PL peaks shown in figure 7(a) and 9. This similarity, analogously to what previously found for the electrical excitation of Si ncs [101], strongly supports the view that both optical and electrical excitation involve as emitting centres quantum confined Si NWs. The intensity fluctuations which characterize the EL spectra with respect to the PL ones are interference phenomena due to the presence of the AZO overlayer. The integrated EL intensity as a function of the applied voltage is plotted in figure 22(b); intensity increases roughly linearly by increasing the voltage and no saturation effects are detected in the investigated voltage range.

8. Conclusions and perspectives

The data reported in this review demonstrate that the use of a nanometric metal layer as the catalyst in the metal-assisted wet etching of Si wafers makes this process able to produce ultrathin Si NWs exhibiting an efficient room temperature PL (an external quantum efficiency of 0.5% has been measured) due to quantum confinement effects. The same process can be effectively used also to produce ultrathin Si/Ge NWs by etching a Si/Ge MQW grown on a Si substrate; these wires, in addition to the room temperature PL signal in the visible range characteristic of Si NWs, exhibit also a low temperature PL signal in the IR region, due to quantum confined Ge nanostructures. The process is maskless, cheap and fast; furthermore, it allows a fine and highly reproducible control of the NW structural properties also over very large areas, up to the wafer scale, demonstrating the applicability of this technique also in an industrial environment.

By looking at practical applications in photonics, it is highly noteworthy that a light emitting device based on conductive Si NWs was successfully realized, exhibiting an intense and stable room temperature EL at very low excitation voltage (2-6 V), just by choosing the doping level of the starting Si substrate; indeed, the electrically active dopant concentration of NWs synthesized by metal-assisted etching processes simply mirrors that of the etched substrate. Therefore, any specific requirement in the concentration or in the nature of the dopant, or the formation of axial p-n junctions, can be very easily and effectively realized through a proper selection of the starting substrate. On the other hand, the doping of NWs grown by VLS-based techniques presents several well-known issues both for in-situ [102] and ex-situ [103] approaches, such as incomplete dopant activation [46], dopant surface segregation [46, 104] or even NW amorphization and bending if ion implantation is used [105]. It is also important to remark that metal inclusion inside the NWs, which is one of the main factors which complicates the application of wires grown by metal-catalysed VLS processes in optical and electrical devices, does not occur by using metal-assisted wet etching. Metal particles are indeed trapped at the bottom of the etched region and can be effectively removed

by a selective etching without the occurrence of diffusion inside the wires, since the whole synthesis works at room temperature.

It is also important to compare performances and perspectives of Si NWs with those of Si ncs which, since the discovery that they can exhibit optical gain [106], are generally recognized as the most promising Si-based material for applications in light sources. Although the two materials show strong similarities from several points of view, NWs probably have a much stronger potential. Si NWs have the great advantage over Si ncs to be a continuous 1D Si system. Si ncs are characterized by a very small volume, and therefore an increase of the electron-hole pairs density leads to a higher probability to have nonradiative Auger processes in competition with the radiative recombination. On the other hand, due to their length, the probability to have nearby electron-hole pairs in NWs is low, and it can be further decreased by increasing their length; as a result, nonradiative phenomena are strongly reduced. By focusing on the electrical excitation, it is well known that direct and Fowler-Nordheim tunnelling are the main conduction mechanism in Si ncs embedded in SiO_2 [101, 107]. These mechanisms involve high operating voltages which complicate device application of this material, since oxide breakdown phenomena often determine the failure of the devices. In contrast, the absence of an embedding insulating matrix and the possibility to conveniently dope the material make Si NWs very good conductors. All the above advantages open the route towards the use of Si NWs as an efficient Si-based light source.

Light emitting Si NWs may open the way to new and unexpected applications in photonics of Si nanostructures; such applications could also benefit from the availability of Si/Ge NWs, where two semiconductors, characterized by different absorption and emission spectra, are put together. In addition, the huge surface area of Si NWs can be effectively exploited for sensing and analytical applications. Just two simple examples have been reported here, but functionalized and NP-decorated NWs are expected to have a great future in many environmental and health applications [108]. Finally, although this aspect is outside the scopes of this review, it is important to remark

also the great potentialities of the dense arrays of NWs synthesized by metal-assisted wet etching as the absorbing medium in third-generation solar cells [30, 109].

Acknowledgements

The authors wish to thank S. Boninelli, M. Galli, V. Fioravanti, F. Pecora, A. Terrasi and G. Impellizzeri for their contribution to some of the experiments reported in this review. We also thank C Percolla, D. Arrigò, G. Lupò for technical assistance. AI acknowledges the projects PON_00214_1 named TECLA.

References

[1] Duan X F, Huang Y, Cui Y, Wang J F and Lieber C M 2001 Indium phosphide nanowires as building blocks for nanoscale electronic and optoelectronic devices *Nature* **409** 66

[2] Tian B, Zheng X, Kempa T J, Fang Y, Yu N, Yu G, Huang J and Lieber C M 2007 Coaxial silicon nanowires as solar cells and nanoelectronic power sources *Nature* **449** 885

[3] Cui Y, Wei Q, Park H and Lieber C M 2001 Nanowire nanosensors for highly sensitive and selective detection of biological and chemical species *Science* **293** 1289

[4] Khriachtchev L 2008 *Silicon Nanophotonics. Basic Principles, Present Status and Perspectives* (Pan Stanford Publishing, Singapore)

[5] Shao M, Cheng L, Zhang M, Ma D D D, Zapien J A, Lee S and Zhang X 2009 Nitrogen-doped silicon nanowires: synthesis and their blue cathodoluminescence and photoluminescence *Appl. Phys. Lett.* **95** 143110

[6] Demichel O, Calvo V, Pauc N, Besson A, Noè P, Oehler F, Gentile P and Magnea N 2009 Recombination dynamics of spatially confined electron-hole system in luminescent gold catalyzed silicon nanowires *Nano Lett.* **9** 2575

[7] Walavalkar S S, Hofmann C E, Homyk A P, Henry M D, Atwater H A and Scherer A 2010 Tunable visible and near-IR emission from sub-10 nm etched single-crystal Si nanopillars *Nano Lett.* **10** 4423

[8] Valenta J, Bruhn B and Linnros J 2011 Coexistence of 1D and quasi-0D photoluminescence from single silicon nanowires *Nano Lett.* **11** 3003

[9] Guichard A R, Barsic D N, Sharma S, Kamins T I and Brongersma M L 2006 Tunable light emission from quantum-confined excitons in $TiSi_2$-catalyzed silicon nanowires *Nano Lett.* **6** 2140

[10] Wagner R S and Ellis W C 1964 Vapor-liquid-solid mechanism of single crystal growth *Appl. Phys. Lett.* **4** 89

[11] Kim B J, Tersoff J, Kodambaka S, Reuter M C, Stach E A and Ross F M 2008 Kinetics of individual nucleation events observed in nanoscale vapor-liquid-solid growth *Science* **322** 1070

[12] Schmidt V, Senz S and Gösele U 2005 Diameter-dependent growth direction of epitaxial silicon nanowires *Nano Lett.* **5** 931

[13] Dayeh S A and Picraux S T 2010 Direct observation of nanoscale size effects in Ge semiconductor nanowire growth *Nano Lett.* **10** 4032

[14] Peng K Q, Wu Y, Fang H, Zhong X Y, Xu Y and Zhu J 2005 Uniform, axial-orientation alignment of one-dimensional single-crystal silicon nanostructure arrays *Angew. Chem.-Int. Ed.* **44** 2737

[15] Huang Z P, Shimizu T, Senz S, Zhang Z, Geyer N and Gösele U 2010 Oxidation rate effect on the direction of metal-assisted chemical and electrochemical etching of silicon *J. Phys. Chem. C* **114** 10683

[16] Peng K, Xu Y, Wu Y, Yan Y, Lee S T and Zhu J 2005 Aligned single-crystalline Si nanowire arrays for photovoltaic applications *Small* **1** 1062

[17] Sivakov V A, Voigt F, Berger A, Bauer G and Christiansen S H 2010 Roughness of silicon nanowire sidewalls and room temperature photoluminescence *Phys. Rev. B* **82** 125446

[18] Cheng S L, Chung C H and Chang Y H 2009 Formation kinetics and structures of high-density vertical Si nanowires on (111)Si substrates *J. Ceram. Process. Res.* **10**, 243

[19] Irrera A, Artoni P, Iacona F, Pecora E F, Franzò G, Galli M, Fazio B, Boninelli S and Priolo F 2012 Quantum confinement and electroluminescence in ultrathin silicon nanowires fabricated by a maskless etching technique *Nanotechnology* **23** 075204

[20] Artoni P, Irrera A, Iacona F, Pecora E F, Franzò G and Priolo F 2012 Temperature dependence and aging effects on silicon nanowires photoluminescence *Opt. Express* **20** 1483

[21] Priolo F, Gregorkiewicz T, Galli M and Krauss T F 2014 Silicon nanostructures for photonics and photovoltaics *Nat. Nanotechnol.* **9** 19

[22] Irrera A, Artoni P, Saija R, Gucciardi P G, Iatì M A, Borghese F, Denti P, Iacona F, Priolo F and Maragò O M 2011 Size-scaling in optical trapping of silicon nanowires *Nano Lett.* **11** 4879

[23] Pecora E F, Lawrence N, Gregg P, Trevino J, Artoni P, Irrera A, Priolo F and Dal Negro L 2012 Nanopatterning of silicon nanowires for enhancing visible photoluminescence *Nanoscale* **4** 2863

[24] Irrera A, Artoni P, Fioravanti V, Franzò G, Fazio B, Musumeci P, Boninelli S, Impellizzeri G, Terrasi A, Priolo F and Iacona F 2014 Visible and infrared emission from Si/Ge nanowires synthesized by metal-assisted wet etching *Nanoscale Res. Lett.* **9** 74

[25] Cioffi N, Picca R A, Lo Faro M J, Calvano C D, Fazio B, Sportelli M C, Trusso S, Ossi P M, Neri F, D'Andrea C and Irrera A 2015 Metal-decorated silicon nanowires for laser desorption-ionization mass spectrometry *SPIE Newsroom* DOI: 10.1117/2.1201509.006086

[26] Li X and Bohn P W 2000 Metal-assisted chemical etching in HF/H_2O_2 produces porous silicon *Appl. Phys. Lett.* **77** 2572

[27] Peng K, Lu A, Zhang R and Lee S T 2008 Motility of metal nanoparticles in silicon and induced anisotropic silicon etching *Adv. Funct. Mater.* **18** 3026

[28] Tzu K, Zhu K, Vinzant T B, Neale N R and Frank A J 2007 Removing structural disorder from oriented TiO_2 nanotube arrays: reducing the dimensionality of transport and recombination in dye-sensitized solar cells *Nano Lett.* **7** 3739

[29] Zhang M-L, Peng K-Q, Fan X, Jie J-S, Zhang R-Q, Lee S-T and Wong N-B 2008 Preparation of large-area uniform silicon nanowires arrays through metal-assisted chemical etching *J. Phys. Chem.* **112** 4444

[30] Fazio B, Artoni P, Iatì M A, D'Andrea C, Lo Faro M J, Del Sorbo S, Pirotta S, Gucciardi P G, Musumeci P, Vasi C S, Saija R, Galli M, Priolo F and Irrera A 2016 Strongly enhanced light trapping in a two-dimensional silicon nanowire random fractal array 2016 *Light-Sci. Appl.* **5** e16062

[31] Khriachtchev L, Räsänen M, Novikov S and Pavesi L 2004 Systematic correlation between Raman spectra, photoluminescence intensity, and absorption coefficient of silica layers containing Si nanocrystals *Appl. Phys. Lett.* **85** 1511

[32] Richter H, Wang Z P and Ley L 1981 The one phonon Raman spectrum in microcrystalline silicon *Solid State Commun.* **39** 625

[33] Campbell I H and Fauchet P M 1986 The effects of microcrystal size and shape on the one phonon Raman spectra of crystalline semiconductors *Solid State Commun.* **58** 739

[34] Piscanec S, Cantoro M, Ferrari A C, Zapien J A, Lifshitz Y, Lee S T, Hofmann S and Robertson J 2003 Raman spectroscopy of silicon nanowires *Phys. Rev. B* **68** 241312

[35] Wang N, Tang Y H, Zhang Y F, Lee C S and Lee S T 1998 Nucleation and growth of Si nanowires from silicon oxide *Phys. Rev. B* **58** R16024

[36] Wang Y, Schmidt V, Senz S and Gösele U 2006 Epitaxial growth of silicon nanowires using an aluminium catalyst *Nat. Nanotechnol.***1** 186

[37] Kamins T I, Williams R S, Basile D B, Hesjedal T and Harris J S 2001 Ti-Catalyzed Si nanowires by chemical vapor deposition: Microscopy and growth mechanism *J. Appl. Phys.* **89** 1008

[38] Stelzner T, Andrä G, Wendler E, Wesch W, Scholz R, Gösele U and Christiansen S 2006 Growth of silicon nanowires by chemical vapour deposition on gold implanted silicon substrates *Nanotechnology* **17** 2895

[39] Iacopi F, Vereecken P M, Schaekers M, Caymax M, Moelans N, Blanpain B, Richard O, Detavernier C and Griffiths H 2007 Plasma-enhanced chemical vapour deposition growth of Si nanowires with low melting point metal catalysts: an effective alternative to Au-mediated growth *Nanotechnology* **18** 505307

[40] Schubert L, Werner P, Zakharov N D, Gerth G, Kolb F M, Long L and Gösele U 2004 Silicon nanowhiskers grown on <111> Si substrates by molecular-beam epitaxy *Appl. Phys. Lett.* **84** 4968

[41] Werner P, Zakharov N D, Gerth G, Schubert L and Gösele U 2006 On the formation of Si nanowires by molecular beam epitaxy *Int. J. Mat. Res.* **97** 1008

[42] Pan Z W, Dai Z R, Xu L, Lee S T and Wang Z L 2001 Temperature-controlled growth of silicon-based nanostructures by thermal evaporation of SiO powders *J. Phys. Chem. B* **105** 2507

[43] Artoni P, Pecora E F, Irrera A and Priolo F 2011 Kinetics of Si and Ge nanowires growth through electron beam evaporation *Nanoscale Res. Lett.* **6** 162

[44] Dubrovskii V G, Sibirev N V, Harmand J C and Glas F 2008 Growth kinetics and crystal structure of semiconductor nanowires. *Phys. Rev. B* **78** 235301

[45] Peng K-Q, Yan Y-J, Gao S-P, Zhu J 2002 Synthesis of large-area silicon nanowire arrays via self-assembling nanoelectrochemistry *Adv. Mater.* **14** 1164

[46] Koren E, Berkovitch N and Rosenwaks Y 2010 Measurement of active dopant distribution and diffusion in individual silicon nanowires *Nano Lett.* **10** 1163

[47] Perea D, Hemesath E R, Schwalbach E J, Lensch-Falk J L, Voorhees P W and Lauhon L J 2009 Direct measurement of dopant distribution in an individual vapour–liquid–solid nanowire *Nat. Nanotechnol.* **4** 315

[48] Ho J-W, Wee Q, Dumond J, Tay A and Chua S-J 2013 Versatile pattern generation of periodic, high aspect ratio Si nanostructure arrays with sub-50-nm resolution on a wafer scale *Nanoscale Res. Lett.* **8** 506

[49] Peng K, Yan Y, Gao S and Zhu J 2003 Dendrite-assisted growth of silicon nanowires in electroless metal deposition, *Adv. Funct. Mater*. **13** 127

[50] Fan Z, Zhang W, Fu Y, Yan L and Ma X 2016 Facile synthesis of silicon micropillar arrays using extreme ultraviolet lithography and Ag-assisted chemical etching method *J. Phys. Chem. C* **120** 6824

[51] Huang Z Geyer N, Werner P, de Boor J and Gösele U 2011 Metal-assisted chemical etching of silicon: a review *Adv. Mater.* **23** 285

[52] Chang S-W, Chuang V P, Boles S T and Thompson C V 2010 Metal-Catalyzed etching of vertically aligned polysilicon and amorphous silicon nanowire arrays by etching direction confinement *Adv. Funct. Mater*. **20** 4364

[53] Huang Z, Zhang X, Reiche M, Liu L, Lee W, Shimizu T, Senz S and Gösele U 2008 Extended arrays of vertically aligned sub-10 nm diameter [100] Si nanowires by metal-assisted chemical etching *Nano Lett.* **8** 3046

[54] Huang Z, Shimizu T, Senz S, Zhang Z, Zhang X, Lee W, Geyer N and Gösele U 2009 Ordered arrays of vertically aligned [110] silicon nanowires by suppressing the crystallographically preferred <100> etching directions *Nano Lett.* **9** 2519

[55] Fang H, Wu Y, Zhao J and Zhu J 2006 Silver catalysis in the fabrication of silicon nanowire arrays *Nanotechnology* **17** 3768

[56] Peng K, Hu J, Yan Y, Wu Y, Fang H, Xu Y, Lee S-T and Zhu J 2006 Fabrication of single-crystalline silicon nanowires by scratching a silicon surface with catalytic metal particles *Adv. Funct. Mater.* **16** 387

[57] Chern W, Hsu K, Chun I S, De Azeredo B P, Ahmed N, Kim K-H, Zuo J-M, Fang N, Ferreira P and Li X 2010 Nonlithographic patterning and metal-assisted chemical etching for manufacturing of tunable light-emitting silicon nanowire arrays *Nano Lett.* **10** 1582

[58] Ghosh R and Giri P K, 2017 Silicon nanowire heterostructures for advanced energy and environmental applications: a review *Nanotechnology* **28** 012001

[59] Katiyar A K, Sinha A K, Manna S and Ray S K 2014 Fabrication of Si/ZnS radial nanowire heterojunction arrays for white light emitting devices on Si substrates *ACS Appl. Mater. Interfaces* **6** 15007

[60] Chan Y F, Su W, Zhang C X, Wu Z L, Tang Y, Sun X Q and Xu H J 2012 Electroluminescence from ZnO-nanofilm/Si-micropillar heterostructure arrays *Opt. Express* **20** 24280

[61] Tan S T, Sun X W, Zhao J L, Iwan S, Cen Z H, Chen T P, Ye J D, Lo G Q, Kwong D L and Teo K L 2008 Ultraviolet and visible electroluminescence from n-ZnO/SiO_x/(n, p)-Si heterostructured light-emitting diodes *Appl. Phys. Lett.* **93** 013506

[62] Yuan-Ming C, Sheng-Rui J, Hsin-Yi L, Chih-Ming L and Jenh-Yih J 2010 Enhanced visible photoluminescence from ultrathin ZnO films grown on Si-nanowires by atomic layer deposition *Nanotechnology* **21** 385705

[63] Moon K-J, Lee T I, Lee W and Myoung J-M 2014 White light emission from heterojunction diodes based on surface-oxidized porous Si nanowire arrays and amorphous In-Ga-Zn-O capping *Nanoscale* **6** 3611

[64] Hsieh Y-P, Chen H-Y, Lin M-Z, Shiu S-C, Hofmann M, Chern M-Y, Jia X, Yang Y-J, Chang H-J, Huang H-M, Tseng S-C, Chen L-C, Chen K-H, Lin C-F, Liang C-. and Chen Y-F 2009 Electroluminescence from ZnO/Si-nanotips light-emitting diodes *Nano Lett.* **9** 1839

[65] Sun L, He H, Liu C, Lu Y and Ye Z 2011 Controllable growth and optical properties of ZnO nanostructures on Si nanowire arrays *Cryst. Eng. Commun.* **13** 2439

[66] Bassu M, Strambini M L, Barillaro G and Fuso F 2010 Light emission from silicon/gold nanoparticles systems *Appl. Phys. Lett*. **97** 143113

[67] Priolo F, Franzò G, Pacifici D, Vinciguerra V, Iacona F and Irrera A 2001 Role of the energy transfer in the optical properties of undoped and Er-doped interacting Si nanocrystals *J. Appl. Phys.* **89** 264

[68] Linnros J, Lalic N, Galeckas A and Grivickas V 1999 Analysis of the stretched exponential photoluminescence decay from nanometer-sized silicon crystals in SiO_2 *J. Appl. Phys.* **86** 6128

[69] Garcia C, Garrido B, Pellegrino P, Ferre R, Moreno J A, Morante J R, Pavesi L and Cazzanelli M 2003 Size dependence of lifetime and absorption cross section of Si nanocrystals embedded in SiO_2 *Appl. Phys. Lett.* **82** 1595

[70] Cullis A G, Canham L T and Calcott P D J 1997 The structural and luminescence properties of porous silicon *J. Appl. Phys.* **82** 909

[71] Dal Negro L, Yi J H, Michel J, Kimerling L C, Chang T-W F, Sukhovatkin V and Sargent E H 2006 Light emission efficiency and dynamics in silicon-rich silicon nitride films *Appl. Phys. Lett.* **88** 233109

[72] Kovalev D, Diener J, Heckler H, Polisski G, Künzner N and Koch F 2000 Optical absorption cross sections of Si nanocrystals *Phys. Rev. B* **61** 4485

[73] Coffa S, Franzò G, Priolo F, Polman A and Serna R 1994 Temperature dependence and quenching processes of the intra-4f luminescence of Er in crystalline Si *Phys. Rev. B* **49** 16313

[74] Brongersma M L, Kik P G, Polman A, Min K S and Atwater H A 2000 Size-dependent electron-hole exchange interaction in Si nanocrystals *Appl. Phys. Lett.* **76** 351

[75] Vinciguerra V, Franzò G, Priolo F, Iacona F and Spinella C 2000 Quantum confinement and recombination dynamics in silicon nanocrystals embedded in Si/SiO_2 superlattices *J. Appl. Phys.* **87** 8165

[76] Calcott P D J, Nash K J, Canham L T, Kane M J and Brumhead D 1993 Identification of radiative transitions in highly porous silicon *J. Phys. Condens. Matter* **5** L91

[77] Palummo M, Iori F, Del Sole R and Ossicini S 2010 Giant excitonic exchange splitting in Si nanowires: first-principles calculations *Phys. Rev. B* **81** 121303

[78] Shim K H, Kil Y-H, Lee H K, Shin M I, Jeong T S, Kang S, Choi C-J and Kim T S 2011 Optical properties of $Si_{0.8}Ge_{0.2}$/Si multiple quantum wells *Mater. Sci. Semicond. Process.* **14** 128

[79] Tayagaki T, Fukatsu S and Kanemitsu Y 2009 Photoluminescence dynamics and reduced Auger recombination in $Si_{1-x}Ge_x$/Si superlattices under high-density photoexcitation *Phys. Rev. B* **79** 041301(R)

[80] Ardyanian M, Rinnert H and Vergnat M 2006 Structure and photoluminescence properties of evaporated GeO_x/SiO_2 multilayers *J. Appl. Phys.* **100** 113106

[81] Julsgaard B, Balling P, Hansen J L, Svane A and Larsen A N 2011 Luminescence decay dynamics of self-assembled germanium islands in silicon *Appl. Phys. Lett.* **98** 093101

[82] Kalem S, Werner P and Talalaev V 2013 Near-IR photoluminescence from Si/Ge nanowire-grown silicon wafers: effect of HF treatment *Appl. Phys. A: Mater. Sci. Process.* **112** 561

[83] Geyer N, Huang Z, Fuhrmann B, Grimm S, Reiche M, Nguyen-Duc T-K, de Boor J, Leipner H S, Werner P and Gösele U 2009 Sub-20 nm Si/Ge superlattice nanowires by metal-assisted etching *Nano Lett.* **9** 3106

[84] Lo Faro M J, D'Andrea C, Messina E, Fazio B, Musumeci P, Reitano R, Franzò G, Gucciardi P G, Vasi C, Priolo F, Iacona F and Irrera A 2015 Silicon nanowire and carbon nanotube hybrid for room temperature multiwavelength light source *Sci. Rep.* **5** 16753

[85] Dillon A C, Gupta P, Robinson M B, Bracker A S and George S M 1990 FTIR studies of water and ammonia decomposition on silicon surfaces *J. Electron Spectrosc. Relat. Phenom.* **54–55** 1085

[86] Brandt M S, Fuchs H D, Stutzmann M, Weber J and Cardona M 1992 The origin of visible luminescence from "porous silicon": a new interpretation *Solid State Commun.* **81** 307

[87] Fazio E, Neri F, D'Andrea C, Ossi P M, Santo N and Trusso S 2011 SERS activity of pulsed laser ablated silver thin films with controlled nanostructure *J. Raman Spectrosc.* **42** 1298

[88] D'Andrea C, Neri F, Ossi P M, Santo N and Trusso S 2009 The controlled pulsed laser deposition of Ag nanoparticle arrays for surface enhanced Raman scattering *Nanotechnology* **20** 245606

[89] Karas M and Hillenkamp F 1988 Laser desorption ionization of proteins with molecular masses exceeding 10,000 daltons *Anal. Chem.* **60** 2299

[90] Law K P and Larkin J 2011 Recent advances in SALDI-MS techniques and their chemical and bioanalytical applications *Anal. Bioanal. Chem.* **399** 2597

[91] Silina Y E and Volmer D A 2013 Nanostructured solid substrates for efficient laser desorption/ionization mass spectrometry (LDI-MS) of low molecular weight compounds *Analyst* **138** 7053

[92] Go E P, Apon J V, Luo G, Saghatelian A, Daniels R H, Sahi V, Dubrow R, Cravatt B F, Vertes A and Siuzdak G 2005 Desorption/ionization on silicon nanowires *Anal. Chem.* **77** 1641

[93] Wei J, Buriak J M and Siuzdak G 1999 Desorption-ionization mass spectrometry on porous silicon *Nature* **399** 243

[94] Piret G, Drobecq H, Coffinier Y, Melnyk O and Boukherroub R 2010 Matrix-free laser desorption/ionization mass spectrometry on silicon nanowire arrays prepared by chemical etching of crystalline silicon *Langmuir* **26** 1354

[95] Dupré M, Enjalbal C, Cantel S, Martinez J, Megouda N, Hadjersi T, Boukherroub R and Coffinier Y 2012 Investigation of silicon-based nanostructure morphology and chemical termination on laser desorption ionization mass spectrometry performance *Anal. Chem.* **84** 10637

[96] Luo G, Chen Y, Daniels H, Dubrow R and Vertes A 2006 Internal energy transfer in laser desorption/ionization from silicon nanowires *J. Phys. Chem. B* **110** 13381

[97] Chen W Y, Huang J T, Cheng Y C, Chien C C and Tsao C W 2011 Fabrication of nanostructured silicon by metal-assisted etching and its effects on matrix-free laser desorption/ionization mass spectrometry *Anal. Chim. Acta* **687** 97

[98] Tsao C-W, Yang Z-J and Chung C-W 2012 Preparation of nanostructured silicon surface for mass spectrometry analysis by an all-wet fabrication process using electroless metal deposition and metal assisted etching *Int. J. Mass Spectrom.* **321-322** 8

[99] Muck A, Stelzner T, Hubner U, Christiansen S and Svatos A 2010 Lithographically patterned silicon nanowire arrays for matrix free LDI-TOF/MS analysis of lipids *Lab. Chip* **10** 320

[100] Picca R A, Calvano C D, Lo Faro M J, Fazio B, Trusso S, Ossi P M, Neri F, D'Andrea C, Irrera A and Cioffi N 2016 Functionalitation of silicon nanowire arrays by silver nanoparticles for the laser desorption ionization mass spectrometry analysis of vegetable oils *J. Mass Spectrom.* **51** 849

[101] Franzò G, Irrera A, Moreira E C, Miritello M, Iacona F, Sanfilippo D, Di Stefano G, Fallica P G and Priolo F 2002 Electroluminescence of silicon nanocrystals in MOS structures *Appl. Phys. A: Mater. Sci. Process.* **74** 1

[102] Schmid H, Björk M T, Knoch J, Karg S, Riel H and Riess W 2009 Doping limits of grown in situ doped silicon nanowires using phosphine *Nano Lett.* **9** 173

[103] Colli A, Fasoli A, Ronning C, Pisana S, Piscanec S and Ferrari A C 2008 Ion beam doping of silicon nanowires *Nano Lett.* **8** 2188

[104] Tutuc E, Appenzeller J, Reuter M C and Guha S 2006 Realization of a linear germanium nanowire p-n junction *Nano Lett.* **6** 2070

[105] Pecora E F, Irrera A, Boninelli S, Romano L, Spinella C and Priolo F 2011 Nanoscale amorphization, bending and recrystallization in silicon nanowires *Appl. Phys. A: Mater. Sci. Process.* **102** 13

[106] Pavesi L, Dal Negro L, Mazzoleni C, Franzò G and Priolo F 2000 Optical gain in silicon nanocrystals *Nature* **408** 440

[107] Anopchenko A, Marconi A, Moser E, Prezioso S, Wang M, Pavesi L, Pucker G and Bellutti P 2009 Low-voltage onset of electroluminescence in nanocrystalline-Si/SiO_2 multilayers *J. Appl. Phys.* **106** 033104

[108] Su Y, Wei X, Peng F, Zhong Y, Lu Y, Su S, Xu T, Lee S-T and He Y 2012 Gold nanoparticles-decorated silicon nanowires as highly efficient near-infrared hyperthermia agents for cancer cells destruction *Nano Lett.* **12** 1845

[109] Sivakov V, Andrä G, Gawlik A, Berger A, Plentz J, Falk F and Christiansen S H 2009 Silicon nanowire-based solar cells on glass: synthesis, optical properties, and cell parameters *Nano Lett.* **9** 1549

FIGURE 1

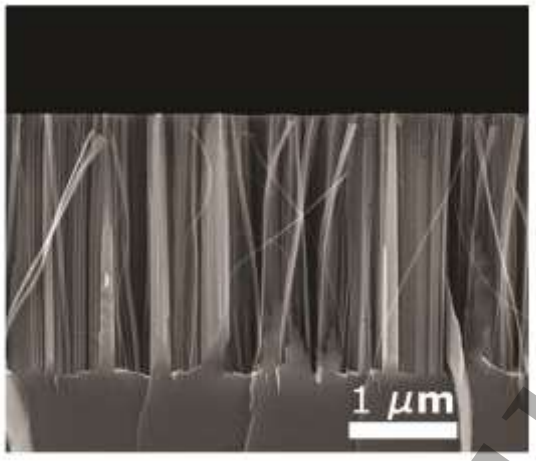

FIGURE 2

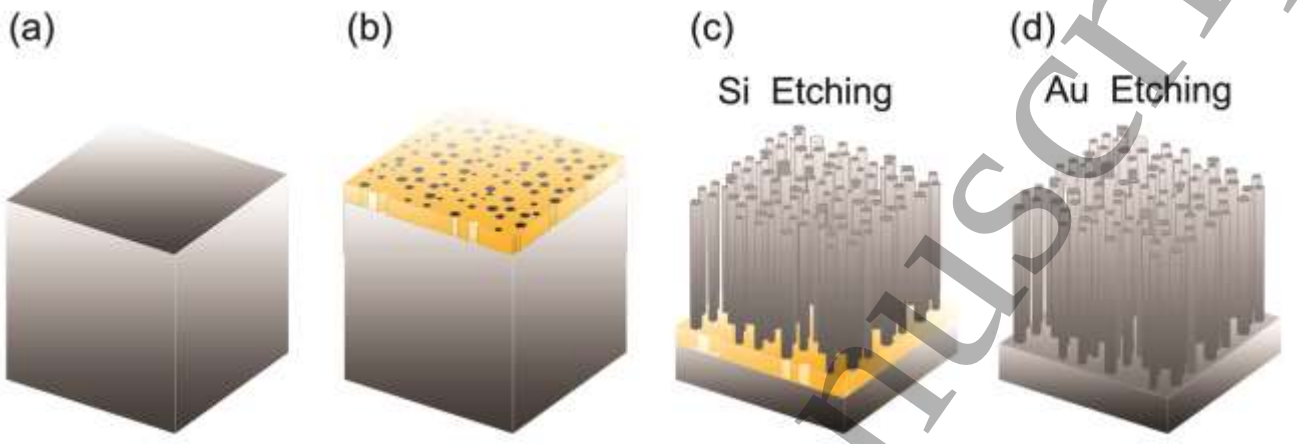

FIGURE 3

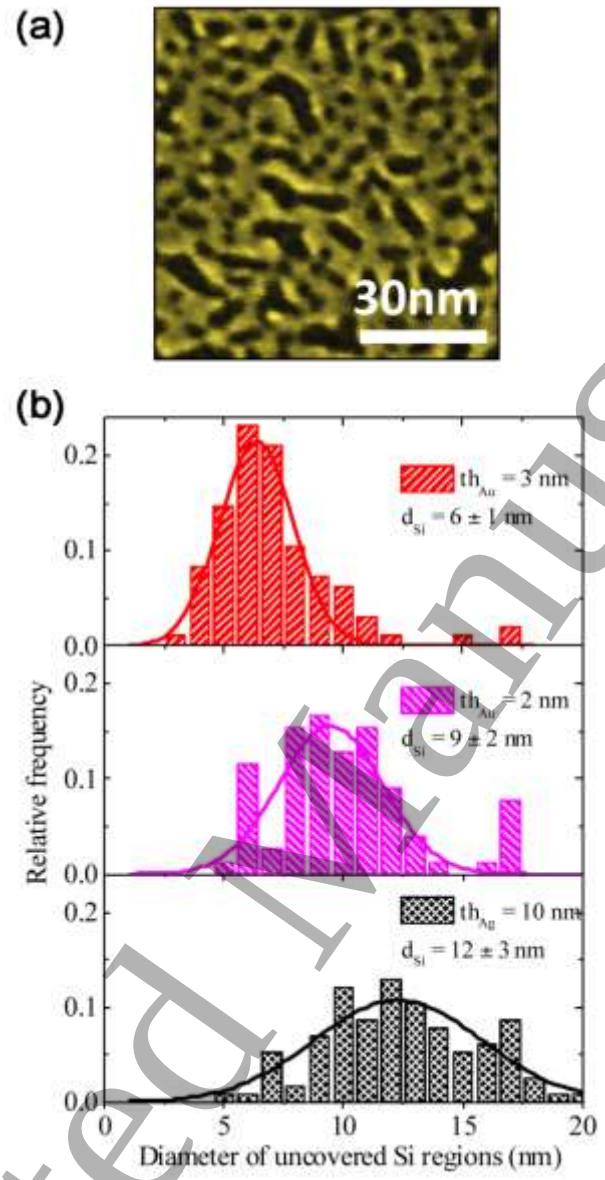

FIGURE 4

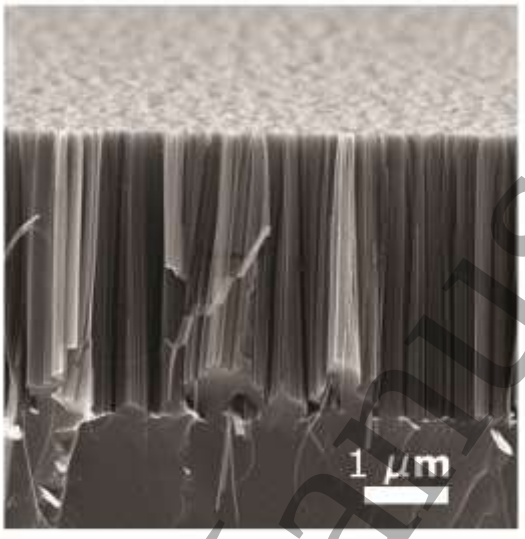

FIGURE 5

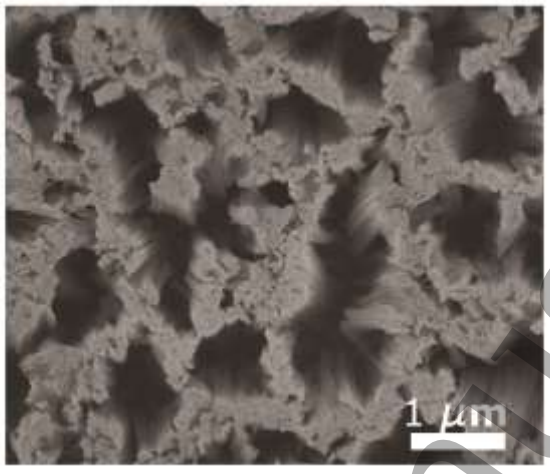

FIGURE 6

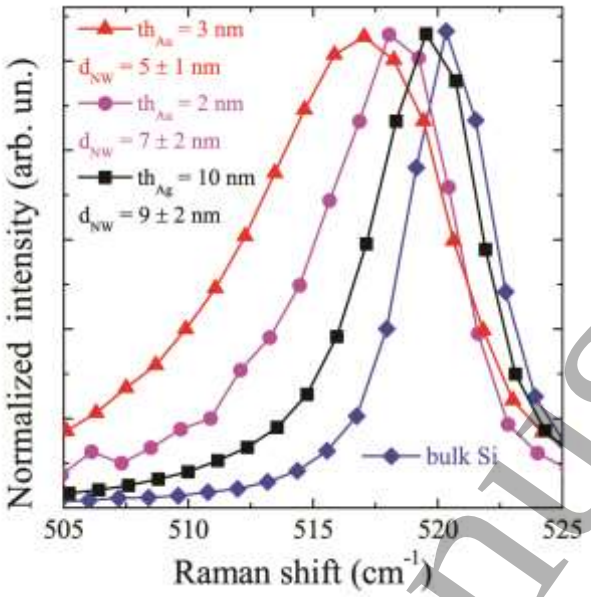

FIGURE 7

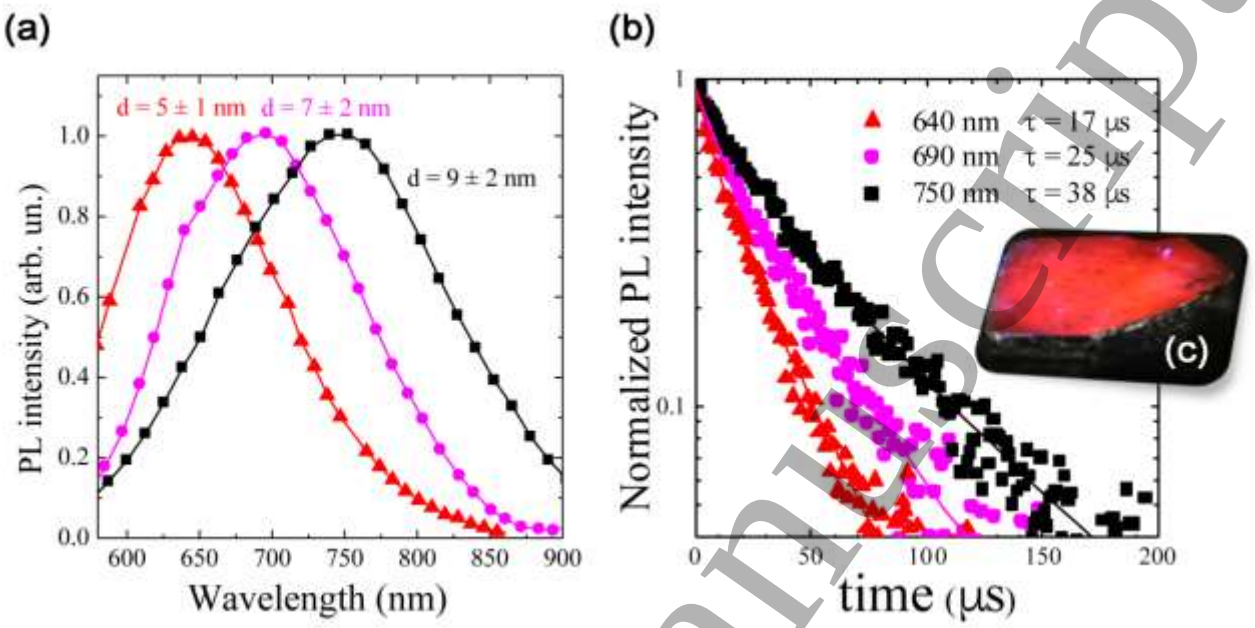

FIGURE 8

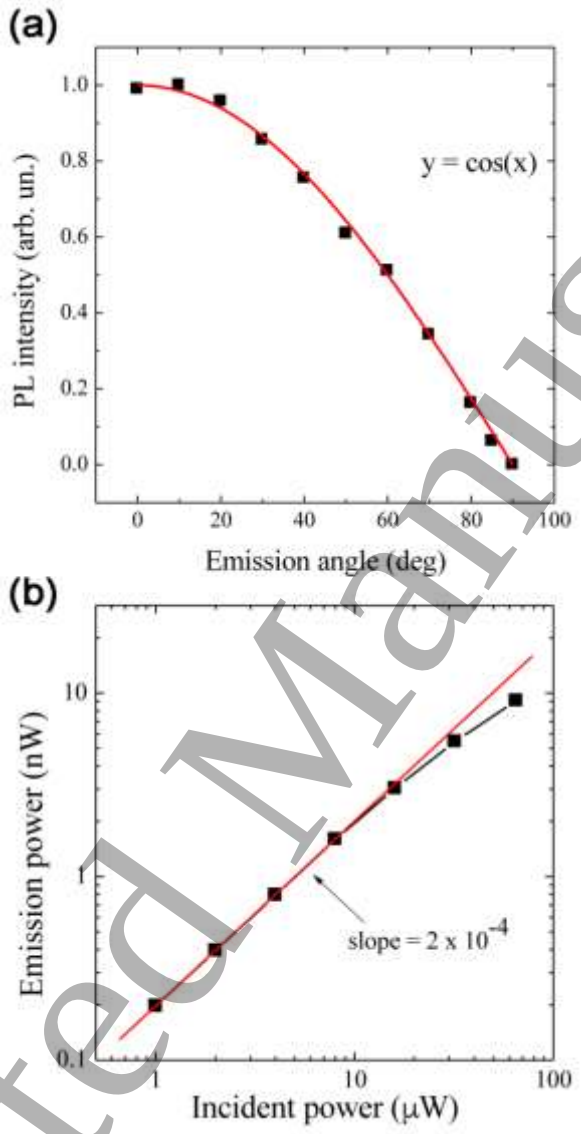

FIGURE 9

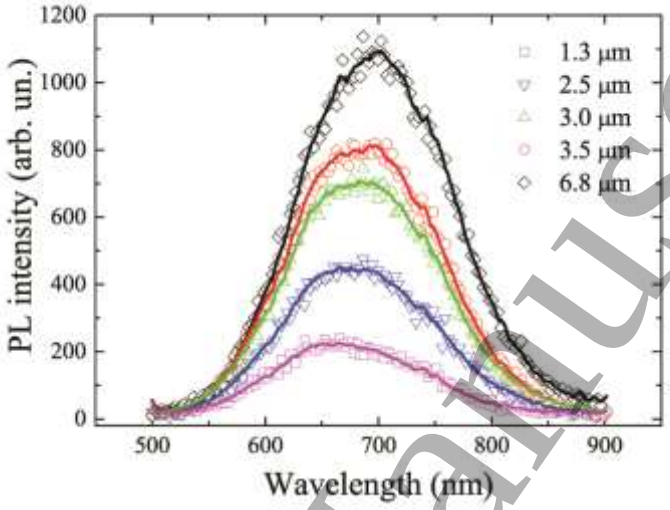

FIGURE 10

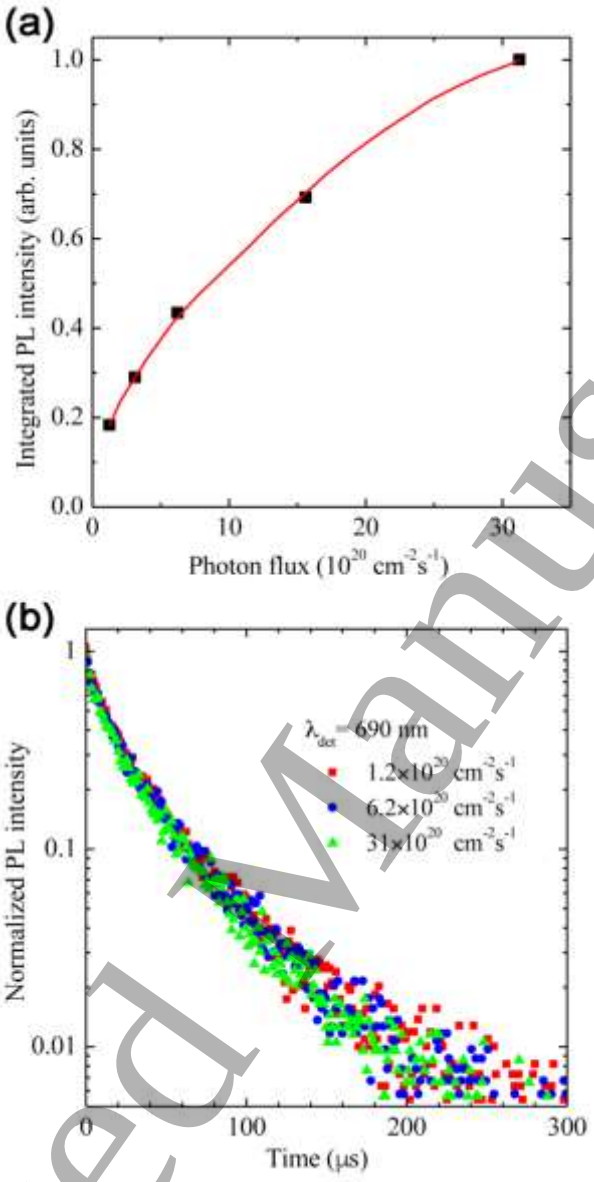

FIGURE 11

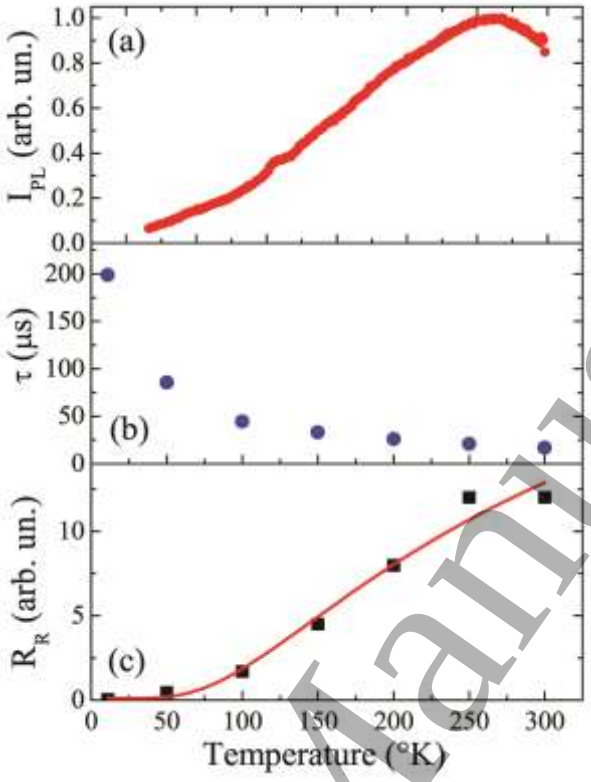

FIGURE 12

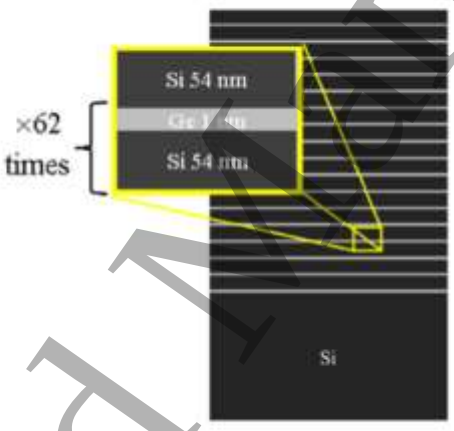

FIGURE 13

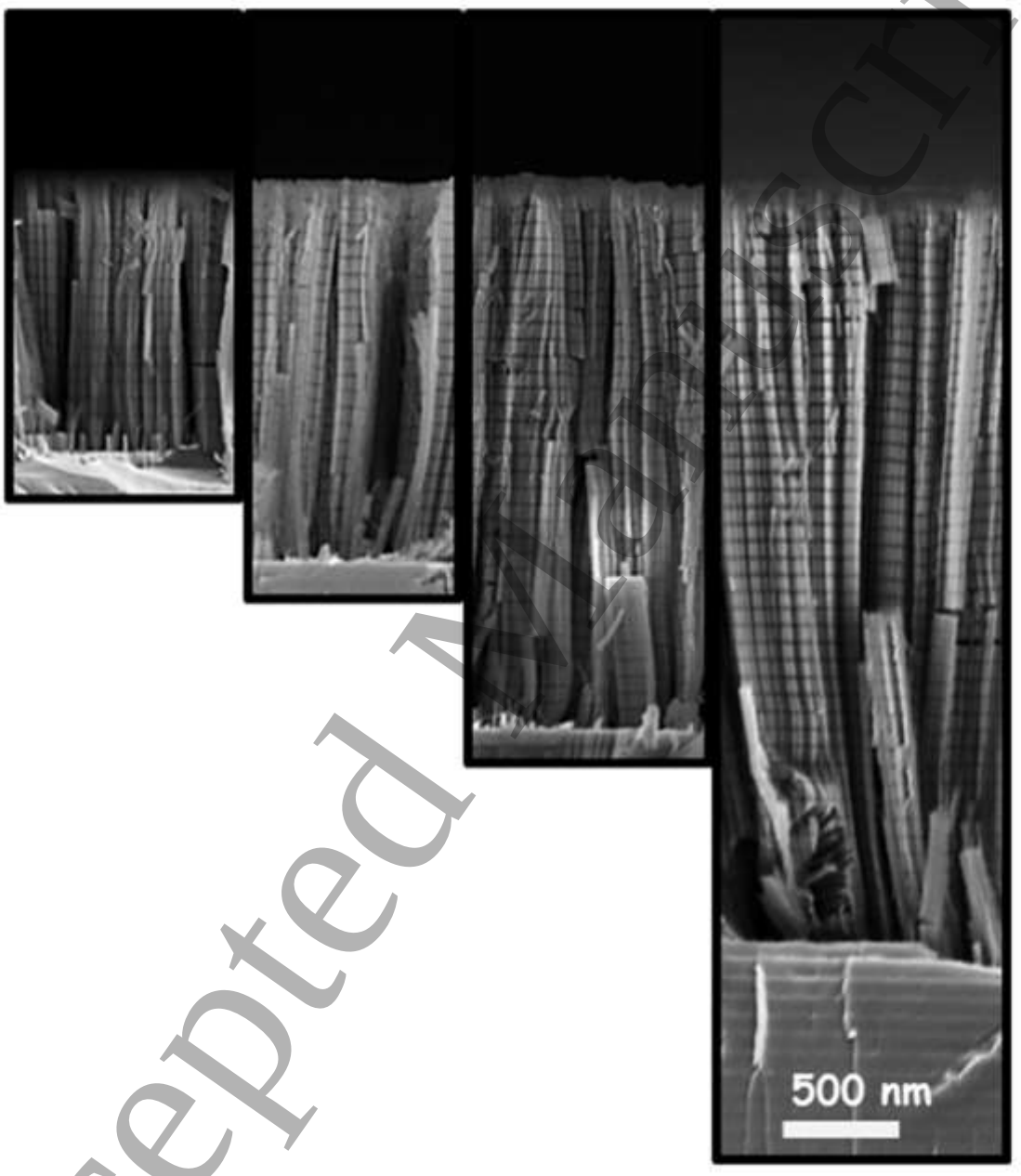

FIGURE 14

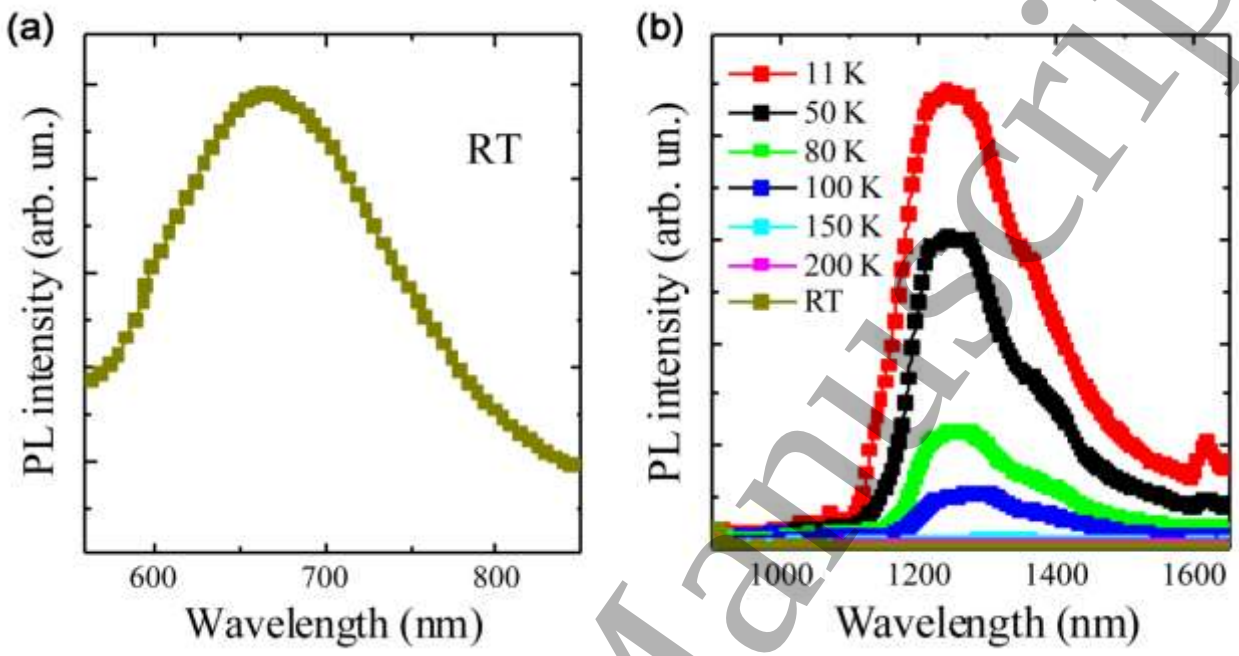

FIGURE 15

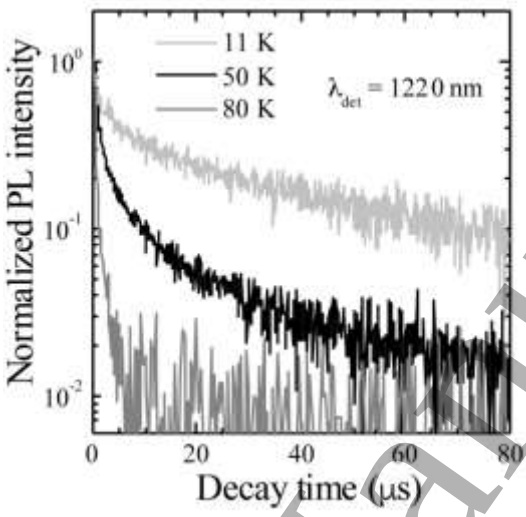

FIGURE 16

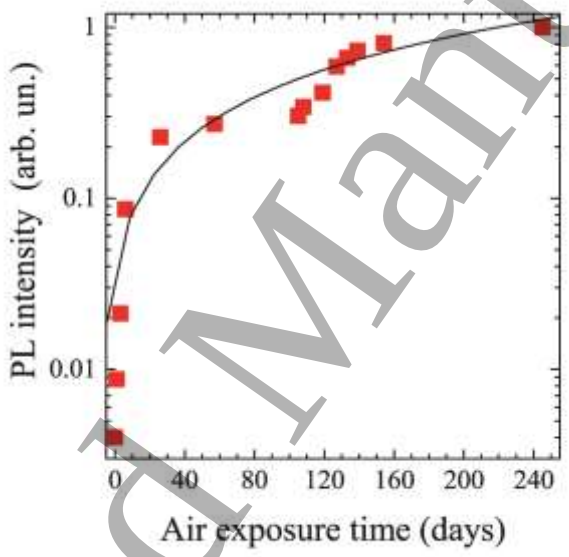

FIGURE 17

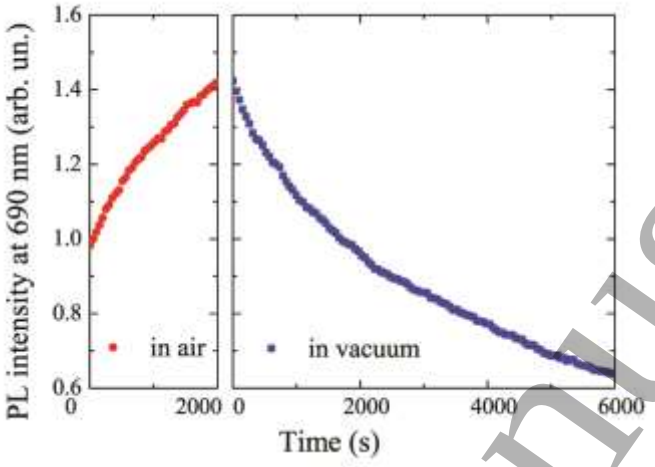

FIGURE 18

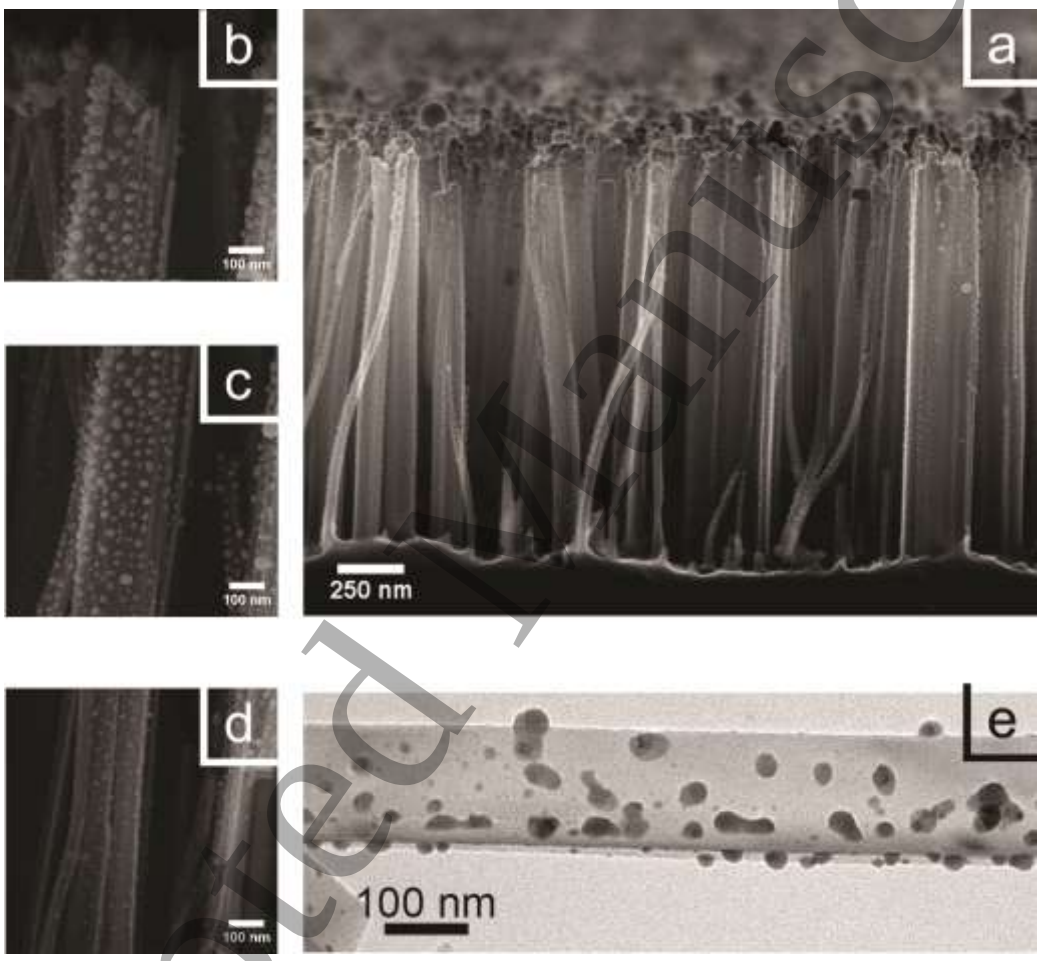

FIGURE 19

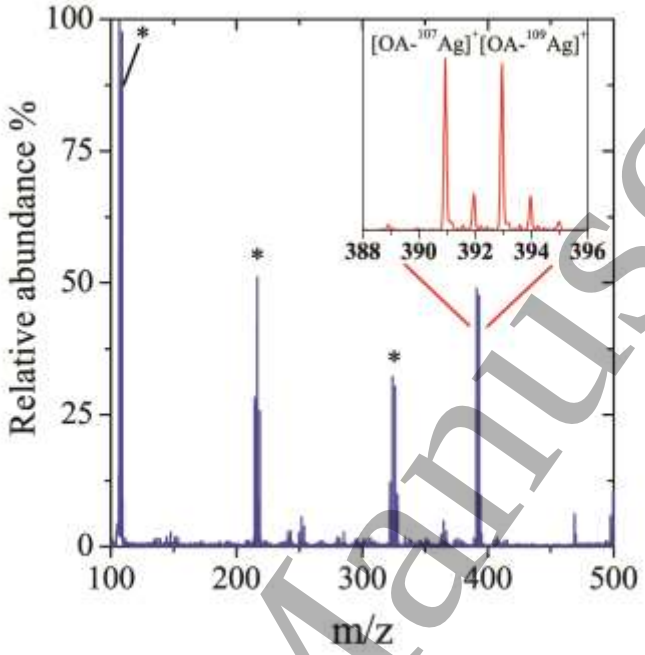

FIGURE 20

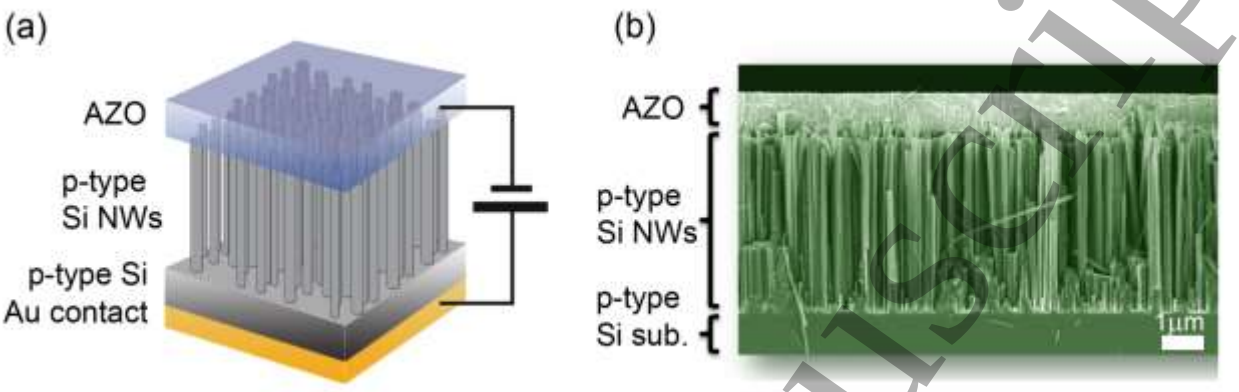

FIGURE 21

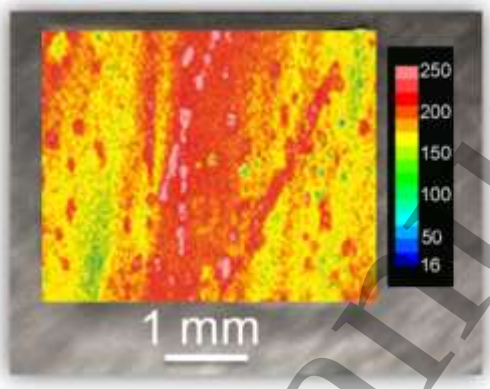

FIGURE 22

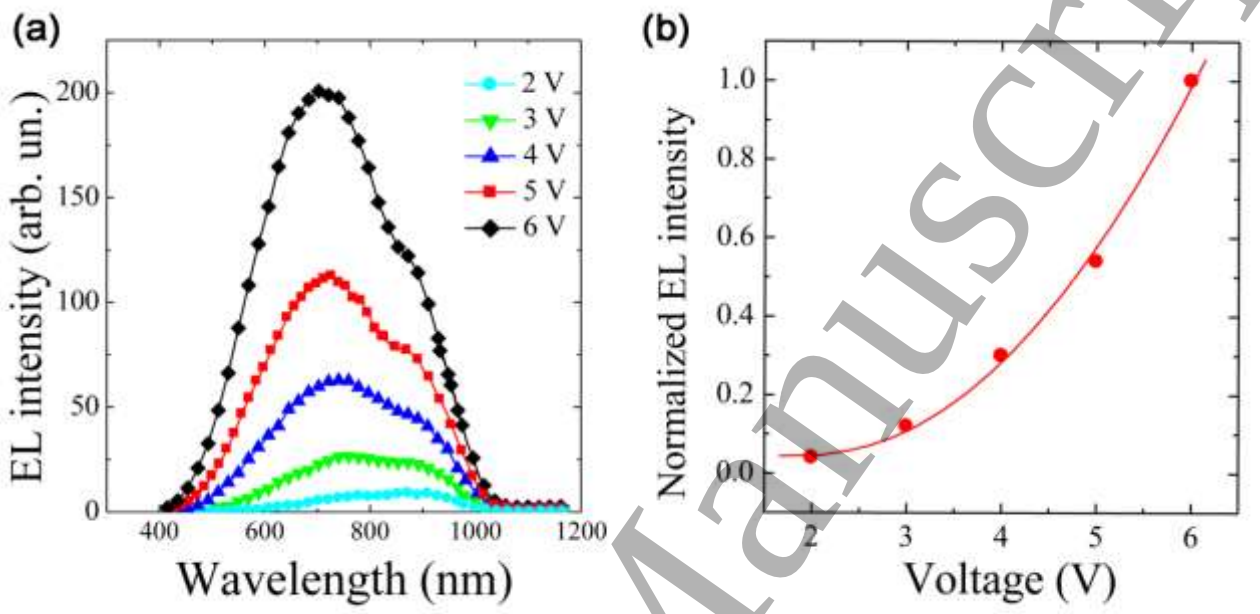

Figure captions

Figure 1. Cross section SEM image displaying a Si NW array synthesized by the metal-assisted wet etching of a Si substrate.

Figure 2. Scheme of the process used for the fabrication of Si NWs. (a) The starting Si substrate. (b) Deposition of a thin metal layer by EBE. (c) Sample etching by an aqueous solution of HF + H_2O_2 and Si NW formation. (d) Removal of the metal layer by an aqueous solution of KI + I_2. All steps are performed at room temperature.

Figure 3. (a) Plan view SEM image of a Si surface after the deposition of a 3 nm thick Au layer. Dark areas are uncovered Si regions while yellowish areas are the nanostructured Au layer. (b) Statistical analysis, based on several SEM images, of the diameter distribution of the circular uncovered Si regions left by the deposition of 2 or 3 nm of Au and of 10 nm of Ag.

Figure 4. Cross section SEM image displaying Si NWs synthesized by metal-assisted wet etching. The sample has been slightly tilted to highlight the extremely high NW areal density (about 1×10^{12} cm^{-2}).

Figure 5. Plan view SEM image of Si NWs synthesized by metal-assisted wet etching.

Figure 6. Raman spectra of Si NWs characterized by different diameters, obtained by using as a catalyst a 3 nm thick Au layer (triangles), a 2 nm thick Au layer (circles), and a 10 nm thick Ag layer (squares). The Raman spectrum of bulk crystalline Si (rhombi) is also shown.

Figure 7. (a) Room temperature PL spectra obtained by exciting Si NWs having different sizes with the 488 line of an Ar^+ laser. (b) PL lifetime of Si NWs at different emitting wavelengths. (c) Photograph of a Si NW sample having an area of about 1 cm^2 excited by the 364 nm line of a fully defocused Ar^+ laser showing a bright red PL emission clearly visible to the naked eye.

Figure 8. (a) Normalized angular dependence of the spectrally integrated PL from Si NWs (squares), as compared to the Lambertian cosine law (line). (b) Power efficiency curve of the light emission from Si NWs. Red line is a linear fit in the low pump power regime.

Figure 9. Room temperature PL spectra of Si NWs with lengths ranging from 1.3 to 6.8 μm, obtained by using an excitation wavelength of 364 nm.

Figure 10. PL properties of Si NWs as a function of the flux of 488 nm photons. (a) Normalized integrated PL intensity. The line is a guide for the eye. (b) Time decay curves of the PL signal measured at 690 nm.

Figure 11. PL properties of Si NWs as a function of the temperature in the range 11–300 K. (a) Normalized intensity of the PL signal at 690 nm. (b) Lifetime of the PL signal, measured at a fixed wavelength of 690 nm. (c) Radiative rate ($R_R = 1/\tau_{rad}$) extracted by the ratio between the PL intensity and the decay time at a fixed photon flux. The line is a fit to the data with $\Delta = 26.9 \pm 4.3$ meV.

Figure 12. A schematic view of the Si/Ge MQW grown by MBE used for Si/Ge NW synthesis.

Figure 13. Cross section SEM images of Si/Ge NWs having lengths ranging from 1.0 to 2.7 μm.

Figure 14. PL spectra of Si/Ge NWs. (a) Room temperature spectrum in the visible region. (b) PL spectra in the IR region, from 11 K to room temperature. The excitation wavelength is 488 nm.

Figure 15. PL time-decay curves of Si/Ge NWs measured at 1220 nm and at temperatures of 11, 50 and 80 K.

Figure 16. Normalized intensity of the PL signal at 690 nm of freshly prepared Si NWs as a function of the air exposure time at room temperature. The line is a linear fit to the data.

Figure 17. Normalized intensity of the PL signal at 690 nm of Si NWs as a function of the exposure time to an Ar^+ laser (488 nm, 10 mW). Data refer to laser irradiation with the sample kept in air (circles) or in vacuum (squares).

Figure 18. (a) Cross section SEM image of a Si NW array decorated with Ag NPs. (b)-(d) High resolution SEM images of the same sample, displaying the uniform coverage, the almost spherical

shape, the high density and the very small size of the NPs in the top, center and bottom region of a decorated NW, respectively. (e) TEM image of an Ag-decorated Si NW.

Figure 19. MS spectrum of oleic acid in acetone obtained using a Si NW array decorated with Ag NPs. Asterisks indicate Ag_n^+ ions (where n = 1, 2, 3) and the inset represents the typical isotopic pattern associated to Ag^+ adducts with oleic acid. *m/z* = mass-to-charge ratio.

Figure 20. (a) Schematic view of an electroluminescent device based on Si NWs. (b) SEM cross section illustrating the device structure. From the top, the AZO layer, the Si NW array and the Si substrate are visible.

Figure 21. EMMI image of a device based on Si NWs**.** The image is in false colors, which are proportional to the PL intensity. The scale of colors is reported in the right part of the figure.

Figure 22. (a) Room temperature EL spectra of a device based on Si NWs, obtained by applying a forward bias in the range 2–6 V. (b) Integrated EL intensity as a function of the applied voltage.